SPOP mutation confers sensitivity to AR-targeted therapy in prostate cancer by reshaping the androgen-driven chromatin landscape

Ivana Grbesa[1,2], Michael A. Augello[1,2,], Deli Liu[1,2,3], Dylan R. McNally[4,5,6], Christopher D. Gaffney[1], Dennis Huang[1,2], Kevin Lin[2], Ramy Goueli[1], Brian D. Robinson[5,7], Francesca Khani[5,7], Lesa D. Deonarine[1,2], Mirjam Blattner[2,7], Olivier Elemento[3,5,7], Elai Davicioni[8], Andrea Sboner[2,3,5,7], Christopher E. Barbieri[1,2,5*]†

[1]Department of Urology, Weill Cornell Medicine, New York, NY 10065, USA.

[2]Sandra and Edward Meyer Cancer Center, Weill Cornell Medicine, New York, NY 10065, USA.

[3]The HRH Prince Alwaleed Bin Talal Bin Abdulaziz Alsaud Institute for Computational Biomedicine, Weill Cornell Medicine, New York, NY 10065, USA.

[4]Department of Physiology and Biophysics, Weill Cornell Medicine, New York, NY 10065, USA.

[5]Caryl and Israel Englander Institute for Precision Medicine, Weill Cornell Medicine, New York, NY 10065, USA.

[6]Department of Medicine and Weill Cornell Cancer Center, Weill Cornell Medicine, New York, NY 10021, USA.

[7]Department of Pathology and Laboratory Medicine, Weill Cornell Medicine, New York, NY 10065, USA.

[8]GenomeDx Bioscience, Vancouver, British Columbia, BC V6B 4X2, Canada.

*To whom correspondence should be addressed: chb9074@med.cornell.edu

†Lead Contact

Keywords: prostate cancer, androgen receptor, FOXA1, organoids, androgen-deprivation therapy, epigenomic landscape

Additional Information

Financial support

This work was funded by: the NCI, US (WCM SPORE in Prostate Cancer, P50CA211024-01, R37CA215040, and R01CA233650, C.E.B.), Damon Runyon Cancer Research Foundation, MetLife Foundation Family Clinical Investigator Award, US (to C.E.B.), and the Prostate Cancer Foundation, US (M.A.A. and D.L.).

Corresponding author

Christopher E. Barbieri

413 E 69th St, New York, NY 10021

Phone: +1 212 746 5562

Fax: 212-746-0975

chb9074@med.cornell.edu

Conflict of interests

C.E.B. is co-inventor on a patent issued to Weill Medical College of Cornell University on SPOP mutations in prostate cancer. E.D. is an employee of GenomeDx, Inc. The authors declare no other potential competing interests.

Data and materials availability

The described RNA-seq, ATAC-seq, and ChIP-seq data have been deposited in NCBI's Gene Expression Omnibus and are accessible through GEO Series accession number GSE145333 (https://www.ncbi.nlm.nih.gov/geo/query/acc.cgi?acc=GSE145333). Reviewer's token is: atypqgkgnlkppoj

Abstract

The normal androgen receptor (AR) cistrome and transcriptional program are fundamentally altered in prostate cancer (PCa). Here, we show that *SPOP* mutations, an early event in prostate tumorigenesis, reshape the chromatin landscape and AR-directed transcriptional program in normal prostate cells. Induction of *SPOP* mutation results in DNA accessibility and AR binding patterns found in human PCa. Consistent with dependency on this AR reprogramming, castration of *SPOP* mutant mouse models results in the loss of neoplastic phenotypes. Finally, human *SPOP* mutant PCa show improved response to AR-targeted therapies. Together, these results show that a single genomic alteration may be sufficient to reprogram the chromatin of normal prostate cells toward oncogenic phenotypes and that *SPOP* mutant tumors may be preferentially dependent on AR signaling through this mechanism.

67 **Introduction**

68 The androgen receptor (AR) is a critical driver and key therapeutic target in prostate cancer
69 (PCa). In normal prostate epithelial cells, AR coordinates growth-suppressive effects and
70 differentiation programs (Heinlein and Chang, 2004; Taplin and Balk, 2004). During prostate
71 carcinogenesis, AR is reprogrammed to instead promote oncogenic transcriptional programs
72 (Pomerantz et al., 2015). However, the mechanisms of this reprogramming remain incompletely
73 understood.

74 Recurrent missense mutations in *SPOP* (Speckle Type BTB/POZ Protein) occur in about
75 10% of localized primary PCa cases (Cancer Genome Atlas Research, 2015; Li et al., 2020) and
76 are highly prostate-specific; they are rarely observed in other cancer types. *SPOP* mutations
77 nominate a distinct molecular subtype of human PCa (Barbieri et al., 2012; Cancer Genome Atlas
78 Research, 2015; Shoag et al., 2018), with defined genomic alterations, DNA methylation,
79 transcriptional signatures, and clinical characteristics (Barbieri et al., 2012; Boysen et al., 2015;
80 Cancer Genome Atlas Research, 2015; Liu et al., 2018). Furthermore, a variety of data suggest
81 that *SPOP* mutations occur early in the process of prostate tumorigenesis (Baca et al., 2013;
82 Boysen et al., 2015). SPOP acts as the substrate recognition component of a CUL3-E3 ubiquitin-
83 protein ligase complex (Zhuang et al., 2009), with prostate cancer-associated mutations affecting
84 substrate specificity. Substrates reported to be affected by *SPOP* mutations include AR itself (An
85 et al., 2014; Geng et al., 2014), the AR coactivators SRC3 (Geng et al., 2013), p300 (Blattner et
86 al., 2017), and TRIM24 (Blattner et al., 2017), and chromatin-associated proteins like DEK
87 (Theurillat et al., 2014) and DAXX (Bouchard et al., 2018). However, how mutations in *SPOP*
88 impact AR-directed transcriptional programs, and if this is required for tumor initiation and
89 progression, remains unclear.

90 Here we leverage the unique capabilities of 3D prostate organoids to define the epigenomic
91 and transcriptional landscape upon AR activation and utilize a genetically engineered mouse
92 (GEM) model conditionally expressing mutant *SPOP* (Blattner et al., 2017) to characterize the
93 impact of a single genomic alteration in genetically normal cells.

94

95 **Results**

96 *Chromatin changes in normal prostate organoids with androgen stimulation*

97 Compared to our understanding of AR function in PCa cell lines and tissues (Pomerantz et
98 al., 2015; Sharma et al., 2013; Stelloo et al., 2018), much less is known of the mechanisms
99 underlying AR-mediated transcriptional regulation in normal prostate cells. Thus, to define the
100 epigenomic response to AR activation, we generated 3D organoid models of murine prostate
101 epithelial cells (Karthaus et al., 2014). Upon establishment, these prostate organoids faithfully
102 mimicked prostate gland architecture (Karthaus et al., 2014) and immunohistochemical features
103 (Fig. S1a). To catalogue the function of AR in the normal prostate, we assessed genome-wide
104 changes in transcriptional profiles (RNA-seq), chromatin accessibility by assay for transposase-
105 accessible chromatin (ATAC-seq), and cistromes of H3K4me2, AR, and FOXA1 by chromatin
106 immunoprecipitation sequencing (ChIP-seq) post-treatment with 10 nM DHT (Fig. 1a).

107 Gene expression data (Fig. S1b) showed upregulation of known murine AR-regulated
108 genes (Carver et al., 2011) by androgens in intact organoids, but not those with CRISPR-mediated
109 deletion of Ar (sgAr). We successfully validated the transcriptional response by performing GSEA
110 on AR-regulated genes in prostate tissue (Carver et al., 2011) (Fig. 1b), confirming a relevant
111 transcriptional response in our organoid model system (Fig. S1 b-f).

112 To define AR-driven alterations in the chromatin landscape in normal prostate epithelial
113 cells, we performed ATAC-seq, as a proxy for genetic regulatory element activity (Fig. S1g-h and
114 Tables S1 and S2). We identified 26,681 high-confidence differentially accessible peaks between
115 DHT-treated and vehicle-treated prostate organoids (FDR < 0.01, Fig. S1i). Next, we performed
116 *de novo* motif analysis of the DHT-enriched versus depleted accessible elements, revealing
117 significant enrichment of the androgen response element (ARE) motif in DHT-treated cells, which
118 was associated with an increase in accessibility at these sites post DHT treatment (Fig. 1c). To
119 connect the DHT-responsive regulatory elements to AR-target genes in prostate tissue, we profiled
120 the ATAC-seq signal of androgen-regulated genes in the mouse prostate (Carver et al., 2011) (Fig.
121 1d). Subsequently, we performed functional enrichment analysis of the ATAC-seq defined DNA
122 regulatory elements and associated AR-induced genes in both prostate organoids and tissue, with
123 "transcription factor binding" and "chromatin (nucleosomal) binding" among the enriched
124 categories (Fig. 1e). Overall, our ATAC-seq analysis confirmed a robust and biologically relevant
125 response to androgens at the chromatin level.

126 Next, to nominate the accessible peaks directly regulated by AR binding, we profiled AR
127 localization genome-wide after DHT stimulation. Genome-wide localization of AR by ChIP-seq
128 resulted in 42,206 AR peaks (Table S1). Importantly, our motif analysis found that the canonical
129 ARE was the most enriched motif in this dataset, confirming the specificity of our signal. Further
130 analysis comparing motif enrichment against that of AR in human prostate tissue (Pomerantz et
131 al., 2015) uncovered a highly similar motif enrichment pattern ($r = 0.89$, $p < 0.001$) (Fig. 1f),
132 suggesting our models faithfully recapitulate critical features of AR signaling.

133 Integrative analysis across data types revealed distinct clusters of regulatory sites either
134 unique to baseline or AR stimulated conditions, or common between these, with associated

135 dominant transcription factors motifs (Fig. 1g, S1e-j). While nuclear hormone receptor motifs were
136 most enriched in dynamic peaks associated with DHT stimulation (cluster 2), regions with
137 chromatin accessibility enriched in basal conditions (cluster 1) or common (cluster 3) were
138 associated with AP-1 motifs (Fra-1 and Jun-B). AP-1 motifs are also common in AR ChIP-seq
139 from normal human prostate tissue (Figure 1f), consistent with an AR-directed role in non-
140 transformed prostate cells.

141 Together, these data demonstrate that androgen stimulation of prostate organoids results in
142 chromatin and transcriptional changes concordant between both murine and human prostate tissues
143 and provides needed insight into the molecular functions of AR in a genetically normal context in
144 addition to being a valuable resource to study early events which contribute to AR driven prostate
145 tumorigenesis. In addition, it is a valuable resource to study early events which contribute to AR
146 driven prostate tumorigenesis.

147

148 *SPOP mutation alone alters the landscape of accessible enhancers in response to androgen*

149 *SPOP* mutations are present in about 10% of PCa (Barbieri et al., 2012; Cancer Genome
150 Atlas Research, 2015; Li et al., 2020), occur early in the natural history of the disease, are relatively
151 prostate-specific, and affect AR activity through deregulation of multiple substrates (Blattner et
152 al., 2017; Geng et al., 2013; Theurillat et al., 2014). We previously developed a transgenic mouse
153 with Cre-dependent, conditional expression of SPOP-F133V (Fig. 2a) (Blattner et al., 2017). In
154 prostate organoids infected with the Cre virus and vector, we examined the impact of an *SPOP*
155 mutation on the epigenomic and transcriptional landscapes after androgen stimulation (Fig. 2b).

156 We profiled the chromatin accessibility landscape of androgen-stimulated prostate
157 organoids expressing mutant (Fig. S2a-c) and wildtype SPOP using ATAC-seq (Fig. S1g-i). We
158 found > 44.9k differentially accessible sites (Fig. 2c), the majority of which were not promoter-
159 associated, but at distal intergenic and intronic regions, consistent with enhancers (Fig. 2d).
160 Dynamic accessible peaks enriched in *SPOP* mutant organoids (Fig. 2e) were enriched for motifs
161 of TFs important for AR-driven prostate tumorigenesis (Fig. 2f), including FOXA1 and HOXB13
162 (Pomerantz et al., 2015). These data support that the chromatin landscape of *SPOP*-mutant prostate
163 cells is remodelled (Fig. S2d-e), especially at androgen-responsive enhancer regions associated
164 with lineage-specific, oncogenic transcription factors.

165 H3K4me2-marked nucleosomes go through remodelling upon AR binding to chromatin
166 (He et al., 2010). Upon androgen stimulation, the H3K4me2 nucleosome at the center of ARE is
167 evicted, and subsequently, AR-binding sites are flanked with H3K4me2 nucleosomes. The same
168 bimodal distribution before and after androgen stimulus was shown in the case of AR-pioneering
169 factor FOXA1 as well (He et al., 2010). Consistent with our chromatin accessibility data, there
170 was more pronounced chromatin remodelling (measured by H3K4me2) at AR bound enhancers in
171 *SPOP*-mutant organoids (Fig. 2g) that also showed a higher frequency of FOXA1 and joint
172 FOXA1:AR motifs.

173

174 *SPOP mutation drives an oncogenic AR-cistrome in prostate organoids*

175 Oncogenic reprogramming of the AR cistrome is a fundamental feature of prostate cancer
176 (Augello et al., 2019; Pomerantz et al., 2015; Sharma et al., 2013; Stelloo et al., 2018), but which
177 specific alterations can drive this phenotype, and what stage of the disease it occurs, remains
178 unclear. We sought to test the hypothesis that a single early event like *SPOP* mutation could impact

179 reprogramming of the AR cistrome to mimic PCa. AR ChIP-seq (Tables S1 and S2) with a
180 validated AR antibody, revealed 13,598 differential AR binding sites (FDR < 0.01) between
181 control and *SPOP*-mutant organoid lines (Fig. 3a). In *SPOP*-mutant organoids, the AR cistrome
182 was enriched for the motifs of well-established regulators of AR function associated with
183 tumorigenesis, including FOXA1 and HOXB13 (Fig. 3b). Strikingly, the motif enrichment pattern
184 in *SPOP*-mutant organoids compared to controls was remarkably similar to that of previously
185 reported in AR cistromes of human prostate adenocarcinoma (PRAD) samples (Pomerantz et al.,
186 2015) as compared to normal prostate tissue (Fig. S3a-b). Consistent with ATAC-seq results, AR
187 peaks in *SPOP*-mutant prostate organoids harbored a higher density of canonical AR and FOXA1
188 motifs (Fig. 3c-d). To validate the relevance of this shift in the TF motif occurrence, we analyzed
189 the AR cistromes of human primary prostate carcinoma tissue samples (Stelloo et al., 2018) (Fig.
190 3e). AR peaks from human *SPOP* mutant cancers had higher FOXA1 motif density (Fig. 3f),
191 associated with a shift in the binding of FOXA1 towards the center of AR peaks (Fig. 3g),
192 consistent with our murine organoid model. Collectively, these data suggest that that *SPOP*
193 mutation alone alters the androgen-responsive enhancer landscape, drives an AR cistrome
194 consistent with PCa, and nominates FOXA1 as a potential mediator of this phenotype.

195

196 *Increased FOXA1 binding in SPOP mutant tumors*

197 FOXA1 acts as a pioneer factor, binding and opening condensed chromatin via its winged-
198 helix DNA binding domains (Cirillo et al., 2002), facilitating AR-mediated transcriptional control
199 (Gao et al., 2003). To better define the role of FOXA1 nominated by motif enrichment in a subset
200 of SPOPmut-specific AR peaks (Fig. 3), we assessed genome-wide FOXA1 binding. *SPOP* mutant
201 organoids and controls showed 27,168 differential FOXA1 peaks (Fig. 4a, Table S1). Moreover,

202 the highest FOXA1, FOXA1:ARE, and ARE motif densities occurred within the SPOPmut-
203 specific FOXA1 cistrome (Fig. 4b). Next, we interrogated AR binding at FOXA1-bound enhancers
204 and found profound enhancement of AR signal at FOXA1-bound accessible enhancers specific for
205 *SPOP* mutant prostate cells (Fig. 4c-d). These data implicate a role for FOXA1 downstream of
206 *SPOP* mutation in driving pro-tumorigenic changes at a subset of AR binding loci.

207 We next looked in human prostate cancers for evidence to support a relationship between
208 *SPOP* mutation and FOXA1. *FOXA1* is recurrently mutated in localized prostate cancer, with
209 forkhead (FKHD) domain mutations altering pioneering activity being the most common (Adams
210 et al., 2019; Barbieri et al., 2012; Cancer Genome Atlas Research, 2015; Parolia et al., 2019). We
211 hypothesized that if *SPOP* mutations acted in part through modulation of FOXA1 activity, then
212 *SPOP*-mutant and *FOXA1*-mutant tumors would display similar features. When applying a
213 previously reported transcriptional classifier for *SPOP* mutation (Liu et al., 2018), the majority of
214 *FOXA*1 mutant tumors cluster together with *SPOP* mutant tumors (Figure 4e). In addition, tumors
215 harbouring *SPOP* mutations and those with *FOXA1* alteration display similar somatic copy number
216 alterations (Figure 4f), suggesting common collaborating events.

217

218 *Gene expression alterations in SPOP mutant prostate organoids*

219 To define whether the changes in accessibility and FOXA1 and AR binding are reflected
220 in transcriptional response to androgens in *SPOP* mutant cells, we performed RNA-seq (Fig. S4a-
221 b). Importantly, AR induced and repressed distinct genes in Control and SPOPmut cells (Fig. 5a).

222 We next sought to leverage multiple levels of data to define genes that are AR-regulated
223 specifically in the context of *SPOP* mutation (Fig. 5b). Integrative analysis of ATAC-seq, AR

224 ChIP-seq, and RNA-seq data nominated genes linked to dynamic regulatory events in *SPOP*
225 mutant mouse organoids, and dependent on AR for induction (n=2043). Of these, 753 genes were
226 also upregulated in *SPOP* mutant human prostate cancers (Fig. 5c), and these were used to generate
227 an *SPOP*-mutant AR signature score (Fig. 5d). By correlating across datatypes, we identified AR-
228 driven, SPOP mutation specific transcriptional regulatory events, with increased AR binding,
229 increased accessibility, and AR-dependent increased gene expression in genes such as *Abcc5* and
230 *Pdlim5*, which has been previously linked to prostate cancer pathogenesis (Liu et al., 2017).
231 Functional categorization of these *SPOP*-mutant specific AR-regulated genes revealed enrichment
232 for metabolic pathways, Nuclear receptor signaling, and cell cycle, consistent with an AR-
233 dependent role in prostate tumorigenesis (Fig. 5f). Together, we conclude that the SPOPmut
234 associated changes in accessibility and transcription factor binding drive a distinct AR-dependent
235 gene expression program, one more consistent with tumorigenesis.

236

237 *Critical dependency of SPOP mutant prostate epithelium on AR signaling*

238 Having observed that *SPOP* mutation alters the androgen-responsive chromatin landscape
239 and transcriptional program, we next examined whether *SPOP* mutant prostate organoids showed
240 increased dependency on AR signaling. *SPOP* mutant organoids showed increased sensitivity to
241 AR inhibition with bicalutamide compared to controls (Fig. 6a), with the proliferation of the
242 SPOPmut significantly more sensitive to anti-androgen treatment both in 2D and 3D growth
243 conditions (Fig. S5a-b). Given the importance of FOXA1 in the epigenomic alterations in *SPOP*-
244 mutant cells, we hypothesized that FOXA1 was necessary for the AR dependency driven by *SPOP*
245 mutation as well. Transient downregulation of FOXA1 further increased the sensitivity of
246 SPOPmut organoids to AR inhibition (Fig. 6b).

247 To investigate the role of AR signaling in a mouse model of *SPOP-F133V*, we performed
248 a pathologic analysis of castrate and hormonally intact mice in a background of heterozygous *Pten*
249 loss ($PbCre^{+};Pten^{L/+};Rosa26^{F133V}$). We have previously shown that *SPOP* mutation alone is
250 insufficient to drive tumorigenesis in mouse prostate (Blattner et al., 2017). However, in a
251 conditional *Pten* deleted background, *SPOP* mutation results in more aggressive neoplastic
252 histology, including high-grade PIN (HG-PIN) in $Pten^{L/+}$ mouse prostates and invasive carcinoma
253 in $Pten^{L/L}$. We castrated *SPOP* mutant ($PbCre^{+};Pten^{L/+};Rosa26^{F133V}$) and control ($PbCre^{+};Pten^{L/+}$)
254 mice at 8 weeks, sacrificed them at 9 months and performed a histological examination of their
255 prostates compared to age-matched uncastrated controls (Fig. 6c). Castration reversed the
256 increased amount of HG-PIN, nuclear atypia, and proliferation seen in *SPOP* mutant prostates
257 compared to controls (Fig. 6d-f and S5c-d). In the setting of homozygous *Pten* loss, *SPOP*-mutant
258 mice ($PbCre^{+};Pten^{L/L};Rosa26^{F133V}$) develop invasive, poorly differentiated carcinomas, while
259 control mice ($PbCre^{+};Pten^{L/L}$) developed only diffuse HG-PIN (Blattner et al., 2017). In this
260 background, we found that *SPOP* mutant castrated mice develop features of invasive disease less
261 frequently than hormonally intact mice, while the diffuse, proliferative HG-PIN in both *SPOP*
262 mutant mice and $Pten^{L/L}$ controls (Fig. 6g) remains relatively castration-resistant, consistent with
263 prior reports (Blattner et al., 2017; Mulholland et al., 2011). Together, these data show that
264 castration results in the reversal of *SPOP* mutant phenotypes *in vivo*, suggesting that these
265 phenotypes are driven by AR signaling.

266

267 *SPOP mutation is associated with improved response to AR-targeted therapies*

268 Given the prominent role of AR signaling in *SPOP* mutant preclinical models, we
269 investigated the impact of *SPOP* mutation on patient response to therapies targeting AR in multiple

clinical scenarios. Using a previously developed transcriptional classifier for the *SPOP* mutant subclass (Liu et al., 2018), we examined data derived from the Decipher Genomics Resource Information Database (GRID) registry (ClinicalTrials.gov identifier: NCT02609269) (Liu et al., 2018). In a pooled retrospective cohort of 1,626 patients *SPOP* mutant tumors were associated with improved metastasis (MET)-free survival in patients who received androgen deprivation therapy (ADT) after radical prostatectomy, but no difference without ADT (Fig. 7a and Table S3). Next, we hypothesized that preferential sensitivity to ADT would manifest with relative depletion of *SPOP* mutant tumors in castrate-resistant prostate cancer compared to hormone-sensitive disease. Comparing 333 primary prostate adenocarcinomas (Cancer Genome Atlas Research, 2015) and 414 metastatic CRPC samples (Abida et al., 2019), *SPOP* mutations were significantly lower in CRPC (Fig. 7b), suggesting a response to ADT. To rule out an effect of primary vs. metastatic disease in this analysis, we compared metastatic hormone-sensitive PCa (mHSPC) to metastatic hormone-resistant PCa (mCRPC) within the same cohort (Abida et al., 2017), and again observed significant underrepresentation of *SPOP* mutation in mCRPC, consistent with the sensitivity of *SPOP* mutant metastatic prostate cancers to ADT (Fig. 7c). Finally, we examined the response of patients with mCRPC patients to AR-targeted therapy (abiraterone and enzalutamide) (Abida et al., 2019). *SPOP* mutation was associated with a longer time on treatment in these patients, suggesting that AR-targeted therapies may be a more durable treatment option in *SPOP* mutant prostate cancer than in other subtypes (Fig. 7d). Overall, all these results together show a favourable outcome of *SPOP* mutant PCa to AR-targeted therapy across multiple clinical scenarios and suggest that *SPOP* mutation may be a predictive biomarker for these therapeutic regimens.

293 **Discussion**

294 The androgen receptor (AR) is the central determinant of prostate tissue identity and
295 differentiation (Cunha et al., 2004), controlling normal, growth-suppressive prostate-specific gene
296 expression (Schiewer et al., 2012). However, it is also a central driver of prostate tumorigenesis,
297 becoming "hijacked" to drive oncogenic transcription (Schiewer et al., 2012). Importantly, it also
298 remains the key therapeutic target for PCa, even in advanced castrate-resistant prostate cancer
299 (CRPC) (Watson et al., 2015). However, how AR function is altered to convert it to an oncogenic
300 factor, and at what steps in the process of tumorigenesis this occurs, remain poorly defined. Here,
301 we show that a single early event in the natural history of prostate cancer is sufficient to drive
302 oncogenic alterations in the AR-directed chromatin landscape and transcriptional program.

303 It has been long recognized that AR is required for the development and function of the
304 normal prostate (Heinlein and Chang, 2004). However, how AR reshapes the landscape of
305 chromatin to execute its transcriptional program, particularly in genetically normal cells, remains
306 unclear. Here, using genetically normal, physiologically relevant prostate organoids, we defined
307 the genome-wide effect of androgens on chromatin accessibility, H3K4me2, AR, and FOXA1
308 binding and subsequent changes in the transcriptome. These data provide insight to transcriptional
309 dynamics of normal AR function, and demonstrate that these genetically pliable models can
310 recapitulate the epigenomic and transcriptomic changes of mouse and human tissue, credentialing
311 a valuable tool to investigate AR activity.

312 Missense mutations in *SPOP* are the most common mutations in primary prostate
313 adenocarcinoma, occur early in the natural history of the disease and affect multiple substrate
314 proteins associated with AR-mediated transcriptional regulation (Blattner et al., 2017; Bouchard
315 et al., 2018; Geng et al., 2013; Geng et al., 2014; Theurillat et al., 2014). Here, we show that *SPOP*

316 mutation alone, in otherwise normal prostate organoids, is sufficient to induce dramatic changes
317 in accessibility of regulatory elements. Furthermore, *SPOP* mutation was sufficient to reprogram
318 the AR cistrome to one with striking resemblance to human PCa. Interestingly one other study
319 reported different effects on the AR cistrome in response to *SPOP* mutation introduced into
320 established cell lines with multiple alterations (Copeland et al., 2019), with expansion of the AR
321 cistrome towards both normal and tumorigenic sites. The more profound shift we report here may
322 reflect the utility of genetically normal models in studying initiation events, and suggest that
323 oncogenic reprogramming of the AR transcriptional program may be a very early event in the
324 natural history of PCa, at least in selected subtypes.

325 FOXA1 is a key pioneering factor for AR and HOXB13 transcription factors, facilitating
326 binding to at PCa-specific AR bound-sites. Furthermore, FOXA1 and HOXB13 overexpression
327 transforms AR cistrome from normal, immortalized cell lines into an oncogenic one (Copeland et
328 al., 2019; Pomerantz et al., 2015). Our study points to a significant role for FOXA1 during the
329 reprogramming of AR cistrome in *SPOP* mutant prostate organoids, consistent with observations
330 in human tumors.

331 The data here suggest that oncogenic reprogramming of AR-driven transcription is the
332 major mechanism underlying the oncogenic function of *SPOP* mutation in prostate cancer.
333 Consistent with this, we also find that functionally, *SPOP* mutant model systems show high
334 dependency on this pathway, and in clinical data, *SPOP* mutant human prostate cancers show
335 increased sensitivity to androgen-targeted therapy. Strikingly, our analysis of the data from
336 multiple clinical scenarios supports this hypothesis: patients receiving adjuvant or salvage ADT
337 after prostatectomy (Fig. 7a) and second generations AR inhibitors with CRPC (Fig. 7d), as well
338 depletion of *SPOP* mutation in CRPC compared to both primary and hormone sensitive metastatic

339 disease (Fig. 7b-c), consistent with reports of favourable outcomes for *SPOP* mutant cancers with
340 therapies targeting AR in both CRPC (Boysen et al., 2018) and hormone sensitive metastatic
341 disease (Swami et al., 2020). However, credentialing *SPOP* mutation as a clinically actionable
342 predictive biomarker for AR-directed therapies will require clinical trials designed for this purpose,
343 likely in each specific clinical scenario. Consistent with this, Tewari and colleagues report that
344 *SPOP* mutation is a truncal alteration in human prostate cancers that show exceptionally robust
345 response to neoadjuvant androgen-targeted therapy (in review). Together, these clinical data
346 suggest that the AR-dependent effects of *SPOP* mutation are not unique to a single clinical
347 scenario, but may extend to multiple stages of prostate cancer, broadening the potential impact.

348

349 **Methods**

350 *Transgenic mouse model*

351 Weill Cornell Medicine (WCM) Institutional Care and Use Committee approved all the
352 mouse studies under protocol 2015-0022. Transgenic mice had prostate-specific expression of
353 human *SPOP-F133V* in *Rosa26* locus (*PbCre;R26*$^{F133V/WT}$ or *PbCre;R26*$^{F133V/F133V}$) with or without
354 *Pten* deletion (*PbCre;R26*$^{F133V/WT}$;*Pten*$^{+/+}$, *PbCre;R26*$^{F133V/WT}$;*Pten*$^{L/+}$,
355 *PbCre;R26*$^{F133V/F133V}$;*Pten*$^{L/+}$ or *PbCre;R26*$^{F133V/WT}$;*Pten*$^{L/L}$)(Blattner et al., 2017). TransNetYX
356 performed mouse genotyping by using published primers (Augello et al., 2019; Blattner et al.,
357 2017).

358

359

360

361 *Immunohistochemistry*

362 Whole murine prostates were processed as previously described(Augello et al., 2019).
363 Staining was done at The Translational Research Program (TRP) of the Department of Pathology
364 and Laboratory Medicine at WCM. Ki67 (ab16667) was used for staining.

365

366 *Murine Organoid Line Generation and CRISPR experiments*

367 Prostate from the *PbCre4* negative; *Rosa26*^{F133V} mice were harvested at 1-2 months of age
368 and processed and grown as 3D Matrigel culture as previously described (Drost et al., 2016) with
369 the exception that the organoid media contained 5 ng/mL EGF. Lines were generated by infection
370 with Adeno-RFP (Control cells) or Adeno-Cre (SPOPmut cells) viruses (Augello et al., 2019). The
371 expression of the human *SPOP-F133V* transgene was confirmed by immunoblot. To knockout *Ar*
372 expression, the cells were infected with lentiviruses containing sgNT or sgAr gRNA in
373 pLentiCRISPRv2 plasmids (a kind gift from Dong Zhao, Sawyer's lab, MSK). Plasmid sequences
374 were verified by Sanger sequencing (Genewiz). Polyclonal populations resistant to puromycin
375 were subjected to immunoblot to verify AR protein expression.

376

377 *Immunofluorescence*

378 Organoids were resuspended Cell Recovery Solution (Corning) to melt the matrigel
379 without disrupting the 3D cellular organization. Organoids were pelleted and embedded into
380 fibrinogen and thrombin clots. These were transferred into embedding cassettes and fixed in 10%
381 formalin. The paraffin sections were prepared at The Translational Research Program of the
382 Department of Pathology and Laboratory Medicine at WCM. Immunofluorescent staining was

383 performed as described previously (Augello et al., 2019) by using anti-Ck5, anti-Ck8, and anti-
384 AR primary antibodies (Blattner et al., 2017).

385

386 *Pathology review*

387 All murine prostate sections were reviewed by board-certified genitourinary pathologists
388 with expertise in human and murine models of prostate cancer (B.D.R., F.K). All reviews were
389 performed blinded to genotype.

390

391 *Immunoblot*

392 Whole-cell protein lysates were prepared after digestion of Matrigel (Corning Cat#
393 356231) with TrypLE Express Enzyme (1X), phenol red (Gibco). Pelleted cells were washed in
394 PBS and lysed in RIPA buffer (Thermo Fisher Scientific, Cat# PI-89901) supplemented with
395 protease and phosphatase inhibitors (Thermo Fisher Scientific, Cat# 78441). Proteins were
396 quantified by BCA assay (Thermo Fisher Scientific, Cat# 23227) and separated on 4-15% Protein
397 Gels (BioRad, Cat# 4568084). SPOP protein was probed by using in-house made rabbit anti-SPOP
398 (1:1000); for AR and FOXA1, we used following rabbit antibodies: Abcam, ab108341 and Abcam,
399 ab23738. For loading control, we used anti-vinculin (ab129002).

400

401 *RNA-seq*

402 Murine organoids were grown for 6 days in media containing 1 nM DHT and then for 24
403 hr without DHT and EGF. Next, cells were stimulated with 10 nM DHT without EGF for 24 hr
404 and harvested for RNA-seq in biological quadruplicates. Total RNA was extracted, and DNaseI

405 treated by Maxwell 16 LEV simplyRNA Cells Kit (Promega, Cat# AS1270) and Maxwell nucleic-
406 acid extraction instrument (Promega). Nanodrop quantified RNA was checked by Bioanalyzer
407 RNA 6000 Nano Kit (Agilent Technologies). Samples with RNA integrity number > 10 were used
408 for library preparation (TruSeq Stranded mRNA Library Preparation (for Poly-A selection and
409 Stranded RNA-Seq) at the WCM Genomics Core. Libraries were sequenced twice on NextSeq500
410 (Illumina), High-output mode to generate 75 bp reads at WCM Genomics Core. Obtained FASTQ
411 files were aligned to the mm10 genome by using STAR v2.4.0j (Dobin et al., 2013). The reads
412 were counted with HTSeq (Anders et al., 2015). Differential gene expression was obtained in R
413 with DESeq2 v1.20.0 package (Anders and Huber, 2010). Gene set enrichment analysis
414 (Subramanian et al., 2005) was run in pre-ranked mode to identify enriched signatures in the
415 Molecular Signature Database (MSigDB).

416

417 *ATAC-seq*

418 Control and SPOPmut organoids were grown and treated as described for the RNA-seq
419 experiment. The experiment was performed in a biological quadruplicate. The single-cell
420 suspension was obtained after digesting organoids in TryPLE. ATAC-seq was performed on
421 100,00 nuclei as previously described (Grbesa et al., 2017) with the minor modifications. Nuclei
422 were isolated in buffer containing 10 mM Tris-Cl pH7.5, 10 mM NaCl, 3 mM $MgCl_2$, 0.1% Tween
423 (Sigma Millipore, Cat # 11332465001), 0.5% NP-40 (Sigma Millipore, Cat # 11332473001),
424 0.01% digitonin (Promega, Cat# G9441) and 1x protease inhibitors. Primers that were used for
425 quality checks of the libraries and for assessing mitochondrial DNA contamination are listed in
426 Table S2. Library size was checked with a Bioanalyzer 2100 system (Agilent Technologies) and
427 High Sensitivity DNA Kit (Agilent Technologies, Cat # 5067-4626). Generated DNA fragments

428 were quantified with Qubit dsDNA HS Assay Kit (Invitrogen, Cat # Q3285). Libraries were pooled
429 at equimolar concentration and submitted to WCM Genomics core, where they were paired-end
430 sequenced on HiSeq 4000 system (Illumina) with 50-bp reads. Raw FASTQ files were pre-
431 processed at WCM Genomics core.

432

433 *Bioinformatic processing of ATAC-seq data*

434 Quality control checks on raw sequence data were done with FASTQC v.0.11.8
435 (http://www.bioinformatics.babraham.ac.uk/projects/fastqc/). Paired-end reads were aligned to the
436 mm10 genome using Bowtie2 v.2.3.4.1 in a very sensitive mode. BAM files were sorted and
437 indexed with SAMtools v.1.8. The percentage of mitochondrial reads (Table S1) was calculated
438 with SAMtools using a custom script. All non-unique reads and mitochondrial reads were removed
439 before peak calling. Bigwig files were generated with deepTools v.3.3.1 (Ramirez et al., 2016)
440 bamCoverage tools from reads with min. mapping quality of 10 and using RPGC normalization.
441 Generated bigwig files were visualized with UCSC Genome Browser. Coverage at TSS of RefSeq
442 genes was done with deepTools computeMatrix and plotHeatmap tools (Fig. S1c). The fraction of
443 reads in peaks (FRiP) score was calculated by custom script by using BEDtools2 v.2.27 (Quinlan
444 and Hall, 2010) and reported in Table S1. Data quality was confirmed using Encode guidelines.
445 Peaks were called using Genrich (https://github.com/jsh58/Genrich), as explained on the Harvard
446 Bioinformatics site (https://informatics.fas.harvard.edu/atac-seq-guidelines.html). As an
447 additional quality control metric, we plotted insert size distribution which confirmed nucleosome-
448 free, mono-and di-nucleosomal distribution of the reads (Fig S1d, S2b). Consensus peaks for each
449 cell type and condition from 4 biological replicas were generated with DiffBind v.3.10 package
450 (Ross-Innes et al., 2012). Differential peak identification (in EdgeR (McCarthy et al., 2012), FDR

451 < 0.01), MA plots, and volcano plots were done in the R software environment v.3.6.0 (The R
452 Foundation) by using DiffBind.

453 Assignment of ATAC-seq peaks to genes – One Mb regions around the transcription start
454 sites of selected genes were retrieved through the UCSC Table Browser program. Then they were
455 intersected with the bed file containing ATAC-seq peak regions.

456 Annotation of Genomic Regions – *Cis*-regulatory element analysis of consensus and
457 differential ATAC-seq peaks was performed with the annotatePeaks.pl of Homer v.4.10 software
458 (Heinz et al., 2010). The stacked barplot of enrichment of genomic regions was created in R v3.6.0
459 with a ggplot2 v3.2.1 package.

460 Integration with RNA-seq data –was done via Cistrome-GO webserver (Li et al., 2019).

461

462 *ChIP-seq experiments and bioinformatic data processing*

463 Control and SPOPmut organoids were grown and treated in biological triplicates, as
464 described in the RNA-seq section. For H3K4me2 ChIP single-cell suspension was crosslinked
465 with 1% methanol-free formaldehyde (Thermo Scientific Pierce, Cat #PI-28906) at 37°C. For AR
466 and FOXA1 ChIP organoids were double fixed (Singh et al., 2019) with 2 mM Di(N-succinimidyl)
467 glutarate (Millipore Signal, Cat #80424-5MG-F) and then 1% formaldehyde. Crosslinking was
468 quenched with 125 mM glycine. The crosslinked organoid pellets were snap-frozen and stored at
469 -80 °C until use. Samples were thawed on ice, lysed in 1% SDS containing buffer supplemented
470 with 1x protease and phosphatase inhibitors, and sonicated for 4 x 10 cycles (30 sec on, 30 sec off)
471 in temperature-controlled Bioruptor 300 (Diagenode). Debris was removed by centrifuging at
472 14,000 rpm at 4°C. One percent of the supernatant was saved as input, and the rest was added to

473 antibody-coupled Dynabead Protein A (Thermo Fisher Scientific, Cat #10001D) and incubated
474 overnight rocking at 4 °C. Used antibodies were: anti-H3K4me2 ChIP-grade (ab7766), anti-AR
475 PG-21 (Millipore, Cat # 06-680) and anti-FOXA1 ChIP-grade (ab23738). Chromatin was washed
476 on ice with 2x each standard wash buffers (Low-Salt, High-Salt, and LiCl) and finally with TE.
477 Decrosslinking of input and immunoprecipitated chromatin was performed in buffer containing
478 1% SDS, 0.3M NaCl, and 0.2 mg/mL Proteinase K (Thermo Fisher Scientific, Cat #AM2548) for
479 16 hr at 65 °C. After 2 hr incubation with RNase A (Thermo Fisher Scientific, Cat #EN0531)
480 decrosslinked material was purified with 2 x AMPure XP beads (Beckman Coulter, Cat #A63881)
481 and eluted in 30 µL of 10 mM Tris-Cl, pH 8. The DNA concentration was measured by Qubit
482 dsDNA HS Assay Kit (Thermo Fisher Scientific, Cat # Q32851). Individual ChIP samples were
483 verified by qPCR (primers are listed in Table S2). Libraries were prepared by NEBNext Ultra II
484 DNA Library Prep (New England Biolabs, Cat #E7645S) by using NEBNext Multiplex Oligos for
485 Illumina (New England Biolabs, Cat #E7335S and #E7500S). Library size and presence of
486 adapters was verified by Bioanalyzer HS DNA chips (Agilent Technologies, Cat# 5067-4626).
487 Libraries passing the quality control were pooled and sequenced at WCM Genomics core for 50
488 cycles on HiSeq4000 to generate single-end 50-bp reads. Generated FASTQ files were validated
489 for quality using FastQC v.0.11.8 software and processed with ENCODE ChIP-seq pipeline
490 (https://github.com/ENCODE-DCC/chip-seq-pipeline2). All reads were aligned to mouse genome
491 mm10. Briefly, this pipeline generated an HTML-quality report from which we inferred the overall
492 quality of our ChIP-seq. Only the samples passing the ENCODE-specified NSC, RCS, FRiP, and
493 PBC metrics (Landt et al., 2012) (https://www.encodeproject.org/data-standards/chip-seq/) were
494 included in further data analysis (Table S1). All the peaks were called with MACS2(Zhang et al.,

495 2008) at the p-value threshold of 0.05. Differential peak analysis was performed by DiffBind in
496 EdgeR mode with 0.01 FDR cutoff.

497

498 *Motif Enrichment Analysis*

499 *De novo* and known motif analysis of ATAC-seq and ChIP-seq consensus or differential
500 peaks was done by findMotifsGenome.pl program within Homer v.4.10 software. For the analysis
501 of H3K4me2 peaks, we used -size given option, while for the rest of the data, we analyzed 200 bp
502 region around the peak summit. To determine motif enrichment between two datasets with similar
503 peak numbers, one served as a background (-bg flag) for the other. For the enhancer-specific motif
504 scanning, peaks localized to promoter and 5'UTR were removed before the analysis. To create
505 motif density histograms the analyzed peaks were centered on the specific motif, and the analysis
506 was run by findMotifsGenome.pl in a histogram mode (-hist with 5 bp bin size) and visualized
507 with GraphPad Prism v8.2.1. Motif analysis of human primary prostate tumors (Stelloo et al.,
508 2018) was done as previously described (Augello et al., 2019) with the only difference that the AR
509 peaks were binned according to the presence or absence of *SPOP* mutation. All the other plots
510 were generated in R with ggplot2 v3.2.1 package.

511

512 *Copy number analysis*

513 The copy number alterations of PRAD were downloaded from TCGA portal
514 (https://portal.gdc.cancer.gov/) via gdc-client tool. Fraction of altered cases within *SPOP* and
515 *FOXA1* mutant subclasses were calculated respectively. Segments with log2-ratio >0.3 were
516 defined as genomic amplifications, and log2-ratio < −0.3 were defined as genomic deletions.

517

518 *3D organoid growth assay*

519 Five thousand cells were seeded in 10 µL of matrigel plug (Corning Matrigel Basement
520 Membrane Matrix, Growth Factor Reduced) per well (Corning 96 well assay, flat bottom clear,
521 black, polystyrene plate) in 100 µL of mouse organoid media (Blattner et al., 2017) without EGF
522 and with 0.01 nM DHT. Cells were allowed to form organoids for four days before the
523 bicalutamide treatment. Drug treated cells were assayed for cell viability after four days with
524 CellTiter-Glo 3D assay (Promega), as per manufacturer's instructions. The experiment was
525 repeated for a total of four biological repeats (technical triplicate for each treatment).
526 Luminescence readings (BioTek Synergy Neo microplate reader with Gen5 software) were
527 analyzed with GraphPad Prism 8.2.1 according to the instructions for the analysis of dose-response
528 data.

529

530 *siRNA mediated FOXA1 knockdown*

531 Transient knockdown of *Foxa1* was done by transfecting mouse organoid cells grown on
532 the surface of collagen I coated plates with siRNA (SMARTpool: siGENOME Foxa1 siRNA). For
533 the control, we used the same concentration of scrambled siRNA (siGENOME Non-Targeting
534 Control siRNA Pool). Transfection was done with Lipofectamine RNAiMAX according to the
535 manufacturer's instructions. After four hours media was replaced and cells were lifted and plated
536 into Matrigel plugs. Bicalutamide treatment and cell viability assay were performed as described
537 above.

538

539 *Clinical data analysis*

540 We have developed a novel gene expression signature, classifier SCaPT (Subclass
541 Predictor Based on Transcriptional Data), and decision tree to predict the *SPOP* mutant subclass
542 from RNA gene expression data (Liu et al., 2018). We then classified the *SPOP* mutant subclass
543 in a Decipher retrospective cohort of 1,626 patients (Table S3) (Liu et al., 2018) and evaluated the
544 associations between *SPOP* mutant status and patient outcomes of metastasis mortality with and
545 without ADT treatment based on Kaplan-Meier (KM) analysis.

546 Prevalence of *SPOP* mutation was analyzed on cBioPortal v3.2.0 platform (Cerami et al.,
547 2012) by using the following datasets (accessed on January 2020): Prostate Adenocarcinoma
548 (TCGA, Cell 2015) (Cancer Genome Atlas Research, 2015), Metastatic Prostate Adenocarcinoma
549 (SU2C/PCF Dream Team) (Abida et al., 2019) and Prostate Cancer (MSKCC) (Abida et al., 2017).
550 For time on ADT analysis, patient's data from cBioPortal and GitHub
551 (https://github.com/cBioPortal/datahub/tree/master/public/prad_su2c_2019) were combined in R
552 v3.6.0. KM analysis and plots were done in R using packages survival 2.44-1.1 and survminer
553 v0.4.6.

554

555 **Acknowledgments**

556 We are indebted to prostate cancer patients and families who contributed to this research. We thank
557 Dr. Dawid Nowak (WCM) and Dr. Jonathan E. Shoag (WCM) for helpful discussion. We thank
558 Dr. Daphne Campigli Di Giammartino (WCM) for helpful advice regarding ChIP-seq experiments.
559 We thank Dr. Mark Rubin for his mentorship and guidance in developing these projects and
560 reagents. We thank Weill Cornell Medicine (WCM) Genomics Core Facility, the Biospecimen and

561 Pathology Core of WCM SPORE in Prostate Cancer and Memorial Sloan Kettering Cancer Center
562 cBioPortal. We are grateful to Dr. Eric Klein, Dr. Bruce J. Trock, Dr. R. Jeffrey Karnes and Dr.
563 Robert B. Den for patient data.
564

565 **References**

566 Abida, W., Armenia, J., Gopalan, A., Brennan, R., Walsh, M., Barron, D., Danila, D., Rathkopf,
567 D., Morris, M., Slovin, S.*, et al.* (2017). Prospective Genomic Profiling of Prostate Cancer
568 Across Disease States Reveals Germline and Somatic Alterations That May Affect Clinical
569 Decision Making. JCO Precis Oncol *2017*.

570 Abida, W., Cyrta, J., Heller, G., Prandi, D., Armenia, J., Coleman, I., Cieslik, M., Benelli, M.,
571 Robinson, D., Van Allen, E.M.*, et al.* (2019). Genomic correlates of clinical outcome in
572 advanced prostate cancer. Proc Natl Acad Sci U S A *116*, 11428-11436.

573 Adams, E.J., Karthaus, W.R., Hoover, E., Liu, D.L., Gruet, A., Zhang, Z.D., Cho, H., DiLoreto,
574 R., Chhangawala, S., Liu, Y.*, et al.* (2019). FOXA1 mutations alter pioneering activity,
575 differentiation and prostate cancer phenotypes. Nature *571*, 408-+.

576 An, J., Wang, C., Deng, Y., Yu, L., and Huang, H. (2014). Destruction of full-length androgen
577 receptor by wild-type SPOP, but not prostate-cancer-associated mutants. Cell Rep *6*, 657-669.

578 Anders, S., and Huber, W. (2010). Differential expression analysis for sequence count data.
579 Genome Biol *11*, R106.

580 Anders, S., Pyl, P.T., and Huber, W. (2015). HTSeq--a Python framework to work with high-
581 throughput sequencing data. Bioinformatics *31*, 166-169.

582 Augello, M.A., Liu, D., Deonarine, L.D., Robinson, B.D., Huang, D., Stelloo, S., Blattner, M.,
583 Doane, A.S., Wong, E.W.P., Chen, Y.*, et al.* (2019). CHD1 Loss Alters AR Binding at Lineage-
584 Specific Enhancers and Modulates Distinct Transcriptional Programs to Drive Prostate
585 Tumorigenesis. Cancer Cell *35*, 817-819.

586 Baca, S.C., Prandi, D., Lawrence, M.S., Mosquera, J.M., Romanel, A., Drier, Y., Park, K.,
587 Kitabayashi, N., MacDonald, T.Y., Ghandi, M.*, et al.* (2013). Punctuated evolution of prostate
588 cancer genomes. Cell *153*, 666-677.
589 Barbieri, C.E., Baca, S.C., Lawrence, M.S., Demichelis, F., Blattner, M., Theurillat, J.P., White,
590 T.A., Stojanov, P., Van Allen, E., Stransky, N.*, et al.* (2012). Exome sequencing identifies
591 recurrent SPOP, FOXA1 and MED12 mutations in prostate cancer. Nat Genet *44*, 685-689.
592 Blattner, M., Liu, D., Robinson, B.D., Huang, D., Poliakov, A., Gao, D., Nataraj, S., Deonarine,
593 L.D., Augello, M.A., Sailer, V.*, et al.* (2017). SPOP Mutation Drives Prostate Tumorigenesis In
594 Vivo through Coordinate Regulation of PI3K/mTOR and AR Signaling. Cancer Cell *31*, 436-
595 451.
596 Bouchard, J.J., Otero, J.H., Scott, D.C., Szulc, E., Martin, E.W., Sabri, N., Granata, D., Marzahn,
597 M.R., Lindorff-Larsen, K., Salvatella, X.*, et al.* (2018). Cancer Mutations of the Tumor
598 Suppressor SPOP Disrupt the Formation of Active, Phase-Separated Compartments. Mol Cell
599 *72*, 19-36 e18.
600 Boysen, G., Barbieri, C.E., Prandi, D., Blattner, M., Chae, S.S., Dahija, A., Nataraj, S., Huang,
601 D., Marotz, C., Xu, L.*, et al.* (2015). SPOP mutation leads to genomic instability in prostate
602 cancer. Elife *4*.
603 Boysen, G., Rodrigues, D.N., Rescigno, P., Seed, G., Dolling, D., Riisnaes, R., Crespo, M.,
604 Zafeiriou, Z., Sumanasuriya, S., Bianchini, D.*, et al.* (2018). SPOP-Mutated/CHD1-Deleted
605 Lethal Prostate Cancer and Abiraterone Sensitivity. Clin Cancer Res *24*, 5585-5593.
606 Cancer Genome Atlas Research, N. (2015). The Molecular Taxonomy of Primary Prostate
607 Cancer. Cell *163*, 1011-1025.

608 Carver, B.S., Chapinski, C., Wongvipat, J., Hieronymus, H., Chen, Y., Chandarlapaty, S., Arora,
609 V.K., Le, C., Koutcher, J., Scher, H.*, et al.* (2011). Reciprocal feedback regulation of PI3K and
610 androgen receptor signaling in PTEN-deficient prostate cancer. Cancer Cell *19*, 575-586.
611 Cerami, E., Gao, J., Dogrusoz, U., Gross, B.E., Sumer, S.O., Aksoy, B.A., Jacobsen, A., Byrne,
612 C.J., Heuer, M.L., Larsson, E.*, et al.* (2012). The cBio cancer genomics portal: an open platform
613 for exploring multidimensional cancer genomics data. Cancer Discov *2*, 401-404.
614 Cirillo, L.A., Lin, F.R., Cuesta, I., Friedman, D., Jarnik, M., and Zaret, K.S. (2002). Opening of
615 compacted chromatin by early developmental transcription factors HNF3 (FoxA) and GATA-4.
616 Mol Cell *9*, 279-289.
617 Copeland, B.T., Du, J., Pal, S.K., and Jones, J.O. (2019). Factors that influence the androgen
618 receptor cistrome in benign and malignant prostate cells. Mol Oncol *13*, 2616-2632.
619 Cunha, G.R., Ricke, W., Thomson, A., Marker, P.C., Risbridger, G., Hayward, S.W., Wang,
620 Y.Z., Donjacour, A.A., and Kurita, T. (2004). Hormonal, cellular, and molecular regulation of
621 normal and neoplastic prostatic development. J Steroid Biochem Mol Biol *92*, 221-236.
622 Dobin, A., Davis, C.A., Schlesinger, F., Drenkow, J., Zaleski, C., Jha, S., Batut, P., Chaisson,
623 M., and Gingeras, T.R. (2013). STAR: ultrafast universal RNA-seq aligner. Bioinformatics *29*,
624 15-21.
625 Drost, J., Karthaus, W.R., Gao, D., Driehuis, E., Sawyers, C.L., Chen, Y., and Clevers, H.
626 (2016). Organoid culture systems for prostate epithelial and cancer tissue. Nat Protoc *11*, 347-
627 358.
628 Gao, N., Zhang, J., Rao, M.A., Case, T.C., Mirosevich, J., Wang, Y., Jin, R., Gupta, A., Rennie,
629 P.S., and Matusik, R.J. (2003). The role of hepatocyte nuclear factor-3 alpha (Forkhead Box A1)

630 and androgen receptor in transcriptional regulation of prostatic genes. Mol Endocrinol *17*, 1484-
631 1507.
632 Geng, C., He, B., Xu, L., Barbieri, C.E., Eedunuri, V.K., Chew, S.A., Zimmermann, M., Bond,
633 R., Shou, J., Li, C.*, et al.* (2013). Prostate cancer-associated mutations in speckle-type POZ
634 protein (SPOP) regulate steroid receptor coactivator 3 protein turnover. Proc Natl Acad Sci U S
635 A *110*, 6997-7002.
636 Geng, C., Rajapakshe, K., Shah, S.S., Shou, J., Eedunuri, V.K., Foley, C., Fiskus, W., Rajendran,
637 M., Chew, S.A., Zimmermann, M.*, et al.* (2014). Androgen receptor is the key transcriptional
638 mediator of the tumor suppressor SPOP in prostate cancer. Cancer Res *74*, 5631-5643.
639 Grbesa, I., Tannenbaum, M., Sarusi-Portuguez, A., Schwartz, M., and Hakim, O. (2017).
640 Mapping Genome-wide Accessible Chromatin in Primary Human T Lymphocytes by ATAC-
641 Seq. J Vis Exp.
642 He, H.H., Meyer, C.A., Shin, H., Bailey, S.T., Wei, G., Wang, Q., Zhang, Y., Xu, K., Ni, M.,
643 Lupien, M.*, et al.* (2010). Nucleosome dynamics define transcriptional enhancers. Nat Genet *42*,
644 343-347.
645 Heinlein, C.A., and Chang, C. (2004). Androgen receptor in prostate cancer. Endocr Rev *25*,
646 276-308.
647 Heinz, S., Benner, C., Spann, N., Bertolino, E., Lin, Y.C., Laslo, P., Cheng, J.X., Murre, C.,
648 Singh, H., and Glass, C.K. (2010). Simple combinations of lineage-determining transcription
649 factors prime cis-regulatory elements required for macrophage and B cell identities. Mol Cell *38*,
650 576-589.

651 Hieronymus, H., Lamb, J., Ross, K.N., Peng, X.P., Clement, C., Rodina, A., Nieto, M., Du, J.,
652 Stegmaier, K., Raj, S.M., *et al.* (2006). Gene expression signature-based chemical genomic
653 prediction identifies a novel class of HSP90 pathway modulators. Cancer Cell *10*, 321-330.
654 Karthaus, W.R., Iaquinta, P.J., Drost, J., Gracanin, A., van Boxtel, R., Wongvipat, J., Dowling,
655 C.M., Gao, D., Begthel, H., Sachs, N., *et al.* (2014). Identification of multipotent luminal
656 progenitor cells in human prostate organoid cultures. Cell *159*, 163-175.
657 Landt, S.G., Marinov, G.K., Kundaje, A., Kheradpour, P., Pauli, F., Batzoglou, S., Bernstein,
658 B.E., Bickel, P., Brown, J.B., Cayting, P., *et al.* (2012). ChIP-seq guidelines and practices of the
659 ENCODE and modENCODE consortia. Genome Res *22*, 1813-1831.
660 Li, J., Xu, C., Lee, H.J., Ren, S., Zi, X., Zhang, Z., Wang, H., Yu, Y., Yang, C., Gao, X., *et al.*
661 (2020). A genomic and epigenomic atlas of prostate cancer in Asian populations. Nature *580*, 93-
662 99.
663 Li, S., Wan, C., Zheng, R., Fan, J., Dong, X., Meyer, C.A., and Liu, X.S. (2019). Cistrome-GO: a
664 web server for functional enrichment analysis of transcription factor ChIP-seq peaks. Nucleic
665 Acids Res *47*, W206-W211.
666 Liu, D., Takhar, M., Alshalalfa, M., Erho, N., Shoag, J., Jenkins, R.B., Karnes, R.J., Ross, A.E.,
667 Schaeffer, E.M., Rubin, M.A., *et al.* (2018). Impact of the SPOP Mutant Subtype on the
668 Interpretation of Clinical Parameters in Prostate Cancer. JCO Precis Oncol *2018*.
669 Liu, X., Chen, L., Huang, H., Lv, J.M., Chen, M., Qu, F.J., Pan, X.W., Li, L., Yin, L., Cui, X.G.,
670 *et al.* (2017). High expression of PDLIM5 facilitates cell tumorigenesis and migration by
671 maintaining AMPK activation in prostate cancer. Oncotarget *8*, 98117-98134.

672 McCarthy, D.J., Chen, Y., and Smyth, G.K. (2012). Differential expression analysis of
673 multifactor RNA-Seq experiments with respect to biological variation. Nucleic Acids Res *40*,
674 4288-4297.
675 Mulholland, D.J., Tran, L.M., Li, Y., Cai, H., Morim, A., Wang, S., Plaisier, S., Garraway, I.P.,
676 Huang, J., Graeber, T.G.*, et al.* (2011). Cell autonomous role of PTEN in regulating castration-
677 resistant prostate cancer growth. Cancer Cell *19*, 792-804.
678 Parolia, A., Cieslik, M., Chu, S.C., Xiao, L.B., Ouchi, T., Zhang, Y.P., Wang, X.J., Vats, P.,
679 Cao, X.H., Pitchiaya, S.*, et al.* (2019). Distinct structural classes of activating FOXA1 alterations
680 in advanced prostate cancer. Nature *571*, 413-+.
681 Pomerantz, M.M., Li, F., Takeda, D.Y., Lenci, R., Chonkar, A., Chabot, M., Cejas, P., Vazquez,
682 F., Cook, J., Shivdasani, R.A.*, et al.* (2015). The androgen receptor cistrome is extensively
683 reprogrammed in human prostate tumorigenesis. Nat Genet *47*, 1346-1351.
684 Quinlan, A.R., and Hall, I.M. (2010). BEDTools: a flexible suite of utilities for comparing
685 genomic features. Bioinformatics *26*, 841-842.
686 Ramirez, F., Ryan, D.P., Gruning, B., Bhardwaj, V., Kilpert, F., Richter, A.S., Heyne, S.,
687 Dundar, F., and Manke, T. (2016). deepTools2: a next generation web server for deep-
688 sequencing data analysis. Nucleic Acids Res *44*, W160-165.
689 Ross-Innes, C.S., Stark, R., Teschendorff, A.E., Holmes, K.A., Ali, H.R., Dunning, M.J., Brown,
690 G.D., Gojis, O., Ellis, I.O., Green, A.R.*, et al.* (2012). Differential oestrogen receptor binding is
691 associated with clinical outcome in breast cancer. Nature *481*, 389-393.
692 Schiewer, M.J., Augello, M.A., and Knudsen, K.E. (2012). The AR dependent cell cycle:
693 mechanisms and cancer relevance. Mol Cell Endocrinol *352*, 34-45.

694 Sharma, N.L., Massie, C.E., Ramos-Montoya, A., Zecchini, V., Scott, H.E., Lamb, A.D.,
695 MacArthur, S., Stark, R., Warren, A.Y., Mills, I.G.*, et al.* (2013). The androgen receptor induces
696 a distinct transcriptional program in castration-resistant prostate cancer in man. Cancer Cell *23*,
697 35-47.
698 Shoag, J., Liu, D., Blattner, M., Sboner, A., Park, K., Deonarine, L., Robinson, B.D., Mosquera,
699 J.M., Chen, Y., Rubin, M.A.*, et al.* (2018). SPOP mutation drives prostate neoplasia without
700 stabilizing oncogenic transcription factor ERG. J Clin Invest *128*, 381-386.
701 Singh, A.A., Schuurman, K., Nevedomskaya, E., Stelloo, S., Linder, S., Droog, M., Kim, Y.,
702 Sanders, J., van der Poel, H., Bergman, A.M.*, et al.* (2019). Optimized ChIP-seq method
703 facilitates transcription factor profiling in human tumors. Life Sci Alliance *2*, e201800115.
704 Stelloo, S., Nevedomskaya, E., Kim, Y., Schuurman, K., Valle-Encinas, E., Lobo, J., Krijgsman,
705 O., Peeper, D.S., Chang, S.L., Feng, F.Y.*, et al.* (2018). Integrative epigenetic taxonomy of
706 primary prostate cancer. Nat Commun *9*, 4900.
707 Subramanian, A., Tamayo, P., Mootha, V.K., Mukherjee, S., Ebert, B.L., Gillette, M.A.,
708 Paulovich, A., Pomeroy, S.L., Golub, T.R., Lander, E.S.*, et al.* (2005). Gene set enrichment
709 analysis: a knowledge-based approach for interpreting genome-wide expression profiles. Proc
710 Natl Acad Sci U S A *102*, 15545-15550.
711 Swami, U., Isaacsson Velho, P., Nussenzveig, R., Chipman, J., Sacristan Santos, V., Erickson,
712 S., Dharmaraj, D., Alva, A.S., Vaishampayan, U.N., Esther, J.*, et al.* (2020). Association of
713 SPOP Mutations with Outcomes in Men with De Novo Metastatic Castration-sensitive Prostate
714 Cancer. Eur Urol.
715 Taplin, M.E., and Balk, S.P. (2004). Androgen receptor: a key molecule in the progression of
716 prostate cancer to hormone independence. J Cell Biochem *91*, 483-490.

717 Theurillat, J.P., Udeshi, N.D., Errington, W.J., Svinkina, T., Baca, S.C., Pop, M., Wild, P.J.,
718 Blattner, M., Groner, A.C., Rubin, M.A., *et al.* (2014). Prostate cancer. Ubiquitylome analysis
719 identifies dysregulation of effector substrates in SPOP-mutant prostate cancer. Science *346*, 85-
720 89.
721 Watson, P.A., Arora, V.K., and Sawyers, C.L. (2015). Emerging mechanisms of resistance to
722 androgen receptor inhibitors in prostate cancer. Nat Rev Cancer *15*, 701-711.
723 Zhang, Y., Liu, T., Meyer, C.A., Eeckhoute, J., Johnson, D.S., Bernstein, B.E., Nusbaum, C.,
724 Myers, R.M., Brown, M., Li, W., *et al.* (2008). Model-based analysis of ChIP-Seq (MACS).
725 Genome Biol *9*, R137.
726 Zhuang, M., Calabrese, M.F., Liu, J., Waddell, M.B., Nourse, A., Hammel, M., Miller, D.J.,
727 Walden, H., Duda, D.M., Seyedin, S.N., *et al.* (2009). Structures of SPOP-substrate complexes:
728 insights into molecular architectures of BTB-Cul3 ubiquitin ligases. Mol Cell *36*, 39-50.

729

730

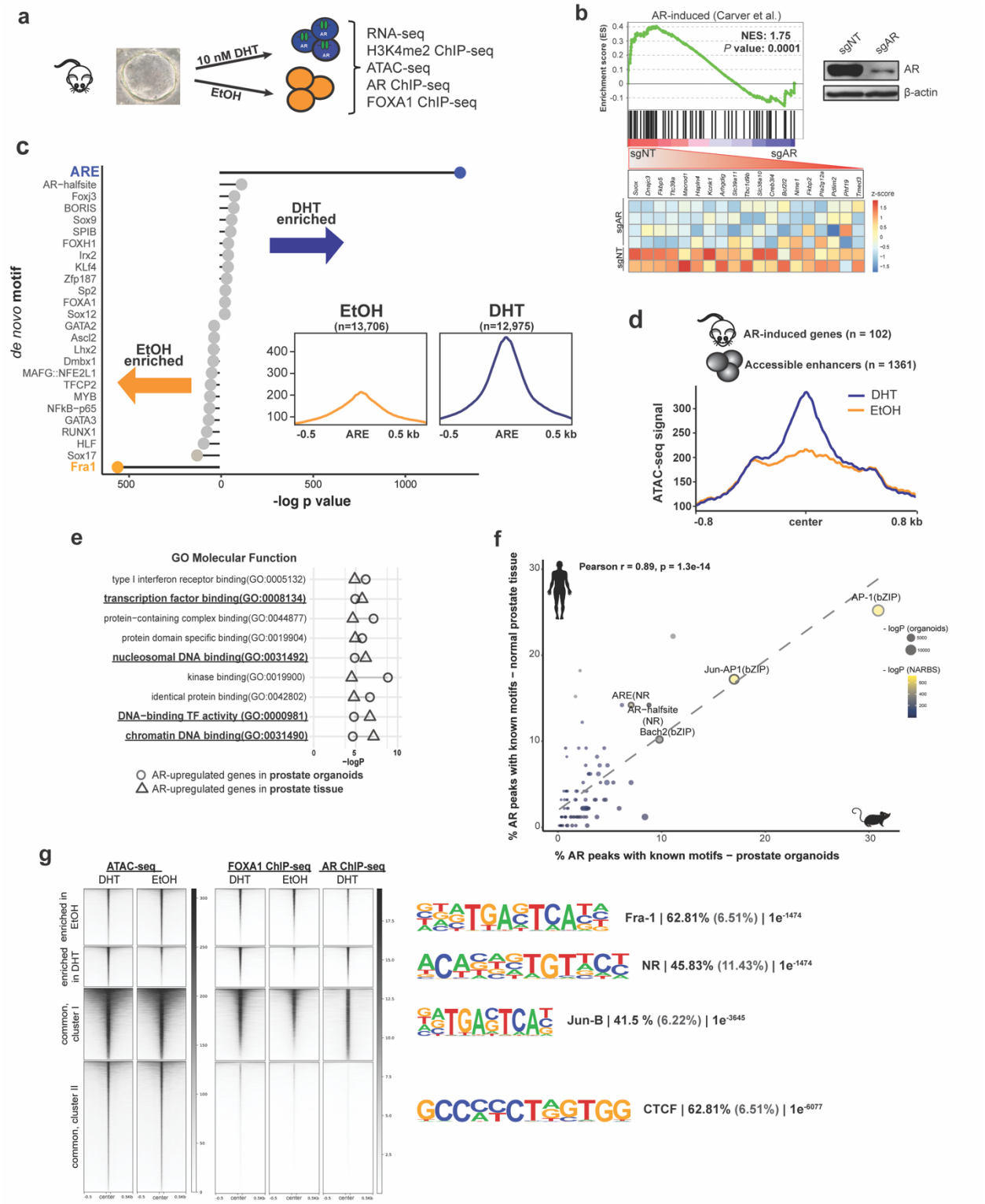

Fig. 1. DHT-induced changes in chromatin accessibility correspond to AR-transcriptional response. (a) Schematic representation of treatments and obtained datasets. **(b)** GSEA and leading

734 edge analysis of AR activity in normal prostate organoids. Upper right corner: Immunoblot of
735 murine organoid CRISPR-Cas9 cells with non-targeting (NT) or *Ar*-specific sgRNA. **(c)** Lolipop
736 plot representing known motif enrichment in vehicle-treated and androgen-treated murine
737 organoids. **(d)** Histogram depicting accessibility signal from EtOH-treated and DHT-treated
738 organoids over the center of regulatory elements within 1 Mb of AR-induced genes from prostate
739 tissue. **(e)** Cleveland plot indicating results of gene ontology (GO) analysis of AR-induced genes
740 in prostate organoids (circle) and prostate tissue (triangles) integrated with accessible regions
741 identified after androgen stimulation of organoid cells. **(f)** Known motif analysis of AR ChIP-seq
742 datasets from normal mouse organoids (x-axis) and human normal prostate tissue (n = 7; GEO:
743 GSE70079; y-axis) demonstrating enrichment for similar motifs ($r = 0.89$, $p < 0.001$). The dotted
744 line represents a regression line. Circle size represents the -log P-value of motif enrichment in AR
745 ChIP-seq peaks in normal murine prostate organoids and circle color the motif enrichment
746 significance in AR binding sites in normal prostate tissue (NARBS). **(g)** ATAC-seq, FOXA1, and
747 AR ChiP-seq signals over the regions that were identified to be more open before (enriched in
748 EtOH) or after androgens (enriched in DHT). The tornado plots also cover the regions whose
749 accessibility is not DHT-dependent (common). The most enriched *de novo* motifs per cluster are
750 depicted on the right, along with the percentage of target (black) and background (grey) regions
751 and the resulting p-value.

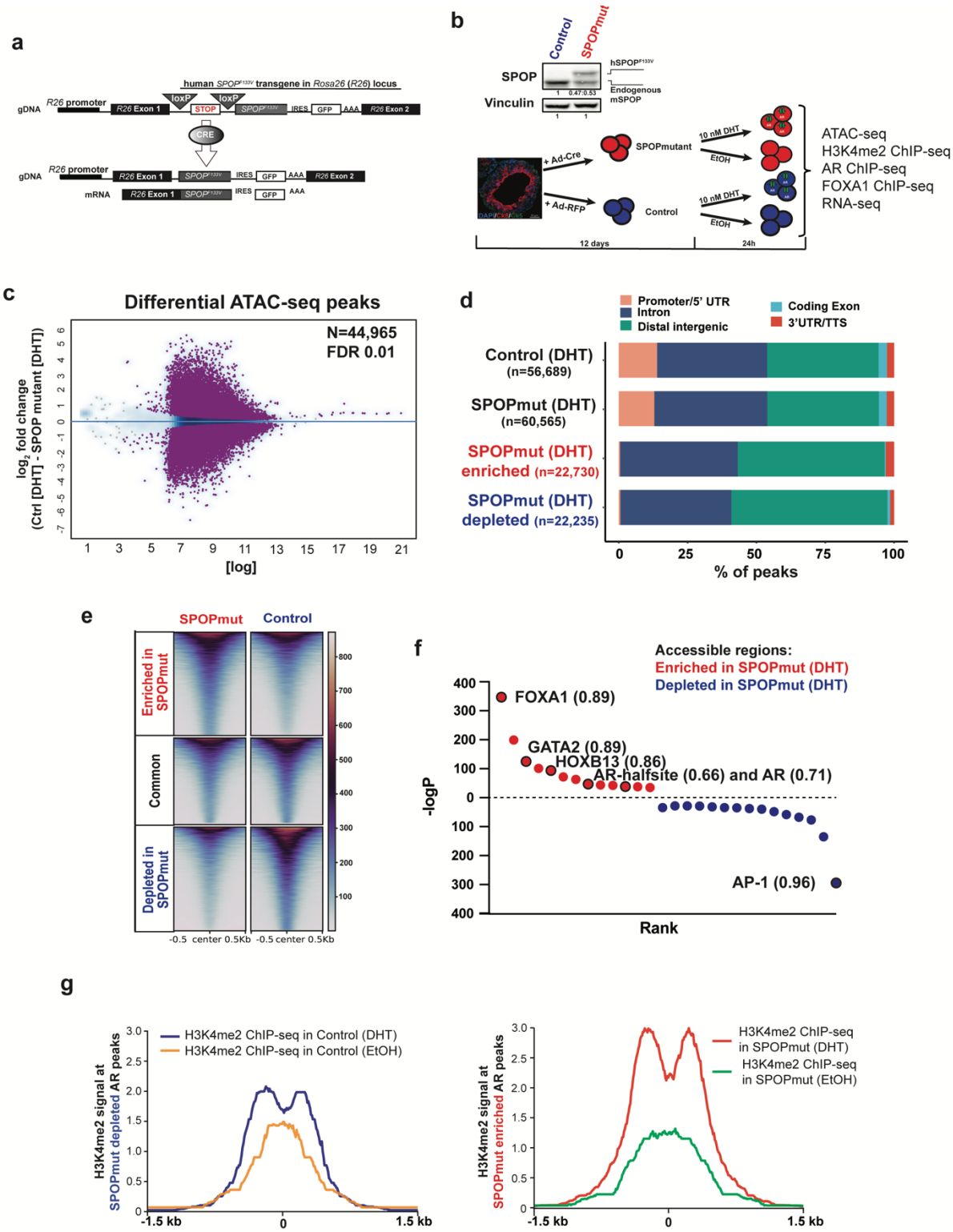

Fig. 2. Extensive remodelling of enhancers in SPOP-mut organoids. (a) Schematic of conditional *SPOP-F133V* construct in the *Rosa26* (*R26*) locus (top) and of the expressed transgenic

755 transcript after Cre introduction (bottom). **(b)** Illustration of the generation of the organoid lines
756 and treatments in addition to all the performed experiments. Up: Immunoblot showing
757 physiological levels of human SPOP-F133V (top band) in comparison to endogenous mouse SPOP
758 protein (bottom band). **(c)** Differential accessible peaks (purple) between Control (n=4) and SPOP-
759 mut (n=4) cells at FDR 0.01. **(d)** Genomic annotation of consensus and differential peaks showing
760 predominant enhancer location of *SPOP* mutant enriched and depleted accessible elements. **(e)**
761 Heatmap of accessible enhancers showing differential accessibility in SPOPmut enriched and
762 depleted peaks. **(f)** *De novo* motif analysis of SPOPmut enriched and depleted accessible DNA
763 regulatory regions. Enriched motifs are plotted according to their rank and *P* value. Values next to
764 the motif are the best match motif score (max. is 1). **(g)** H3K4me2 signal at the enhancers from
765 Control and *SPOP* mutant organoids with and without DHT stimulation at *SPOP* mutant depleted
766 AR peaks (left), and *SPOP* mutant enriched AR peaks (right).
767

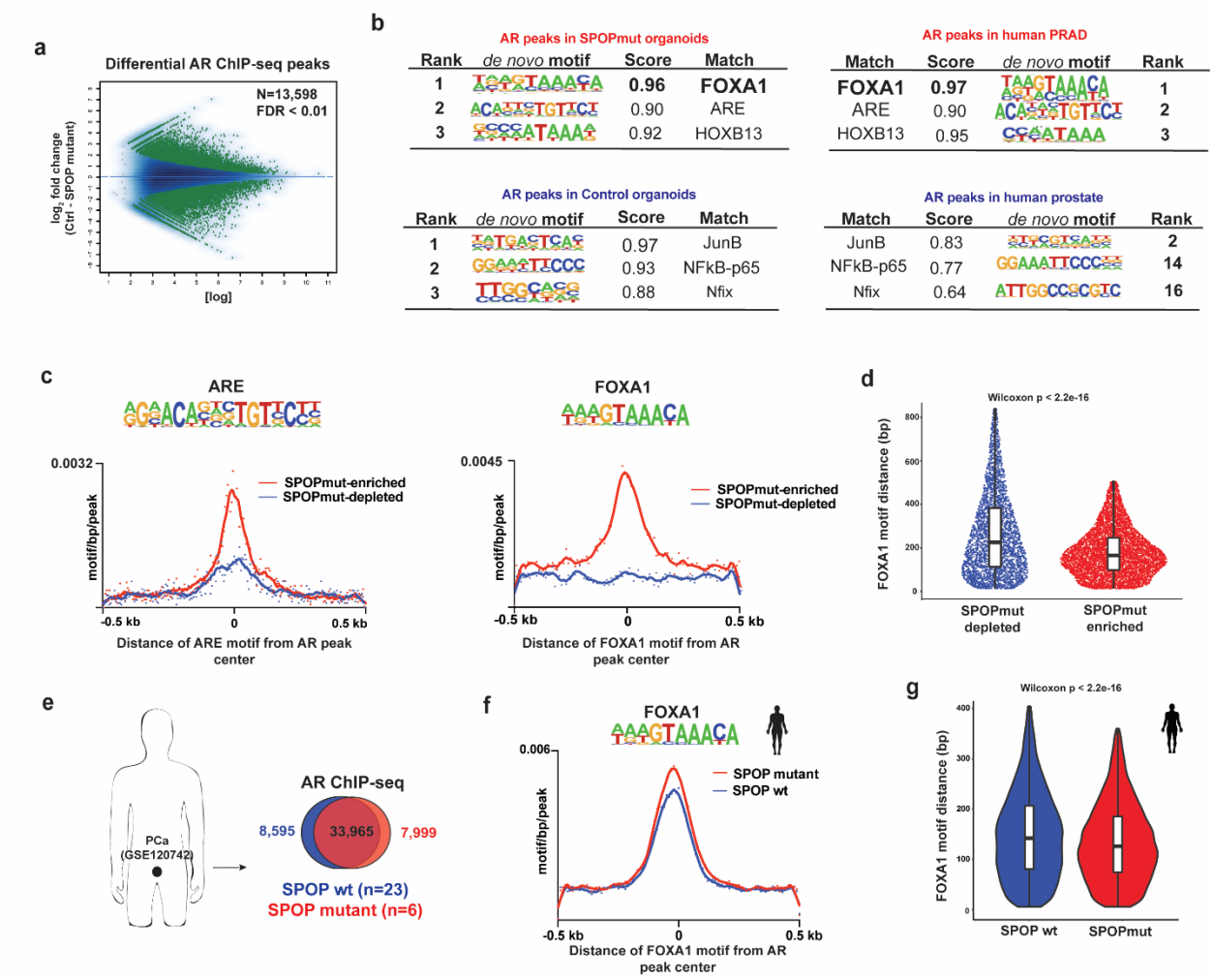

Fig. 3. AR cistrome from *SPOP*-mutated cells is enriched for FOXA1 motifs. (a) MA plot showing AR differential sites (green dots) between Control and SPOP-F133V expressing organoids using two biological replicates per condition. **(b)** *De novo* motif analysis of AR cistrome in SPOPmut and Control organoids (right). Left: the same type of motif analysis performed on human PRAD (Pomerantz et al., 2015). **(c)** Histograms of ARE (left) and FOXA1 (right) motif densities within a 500 bp window around the center of each AR peak. Input files were from *SPOP* mutant enriched (red line) and depleted (blue depleted) AR ChIP-seq peaks. **(d)** Sina plot – distances of FOXA1 motif from the center of each AR peak. Input files were as in (c). **(e)** AR ChIP-seq data from human prostate cancer tissues (Stelloo et al., 2018) (GSE120742). Peaks

778 coming from either PRAD with *SPOP* mutation or wt *SPOP* were merged and intersected. **(f)**
779 Histogram of FOXA1 motif density in AR binding sites from human prostate cells with SPOP-
780 F133V (red line) or wt SPOP (blue). **(g)** The distance of the FOXA1 motif from the center of AR
781 ChIP-seq peaks in each prostate cancer group.

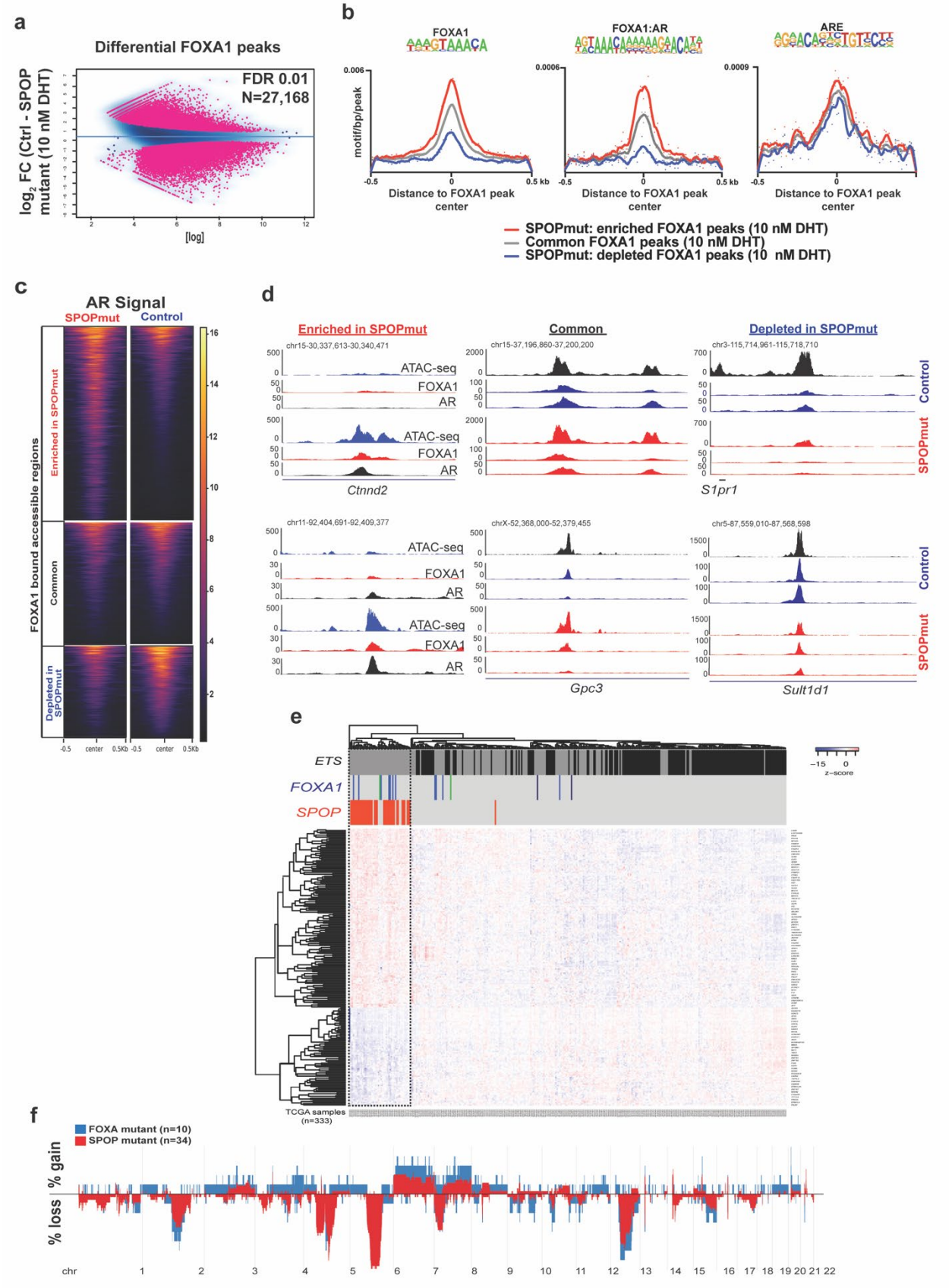
a
Differential FOXA1 peaks
FDR 0.01
N=27,168
log2 FC (Ctrl - SPOP mutant (10 nM DHT))
[log]
b
FOXA1
FOXA1:AR
ARE
motif/bp/peak
Distance to FOXA1 peak center
SPOPmut: enriched FOXA1 peaks (10 nM DHT)
Common FOXA1 peaks (10 nM DHT)
SPOPmut: depleted FOXA1 peaks (10 nM DHT)
c
AR Signal
SPOPmut
Control
FOXA1 bound accessible regions
Enriched in SPOPmut
Common
Depleted in SPOPmut
d
Enriched in SPOPmut
Common
Depleted in SPOPmut
ATAC-seq
FOXA1
AR
Control
SPOPmut
Ctnnd2
S1pr1
Gpc3
Sult1d1
e
ETS
FOXA1
SPOP
z-score
TCGA samples (n=333)
f
FOXA mutant (n=10)
SPOP mutant (n=34)
% gain
% loss
chr

782

783 **Fig. 4.** Increased binding of FOXA1 at *SPOP* mutant-specific AR sites. **(a)** Differential FOXA1
784 genome-wide binding in Control (n=2) and *SPOP* mutant (n=2) organoids upon AR activation. **(b)**
785 Motif densities within the center of FOXA1 peaks enriched (red) or depleted (blue) in *SPOP*
786 mutant murine organoids. Gray - The signal at regions where FOXA1 binding intensity does not
787 change. **(c)** AR binding signal at FOXA1-bound DNA regulatory elements that are common
788 between the lines or *SPOP* mutant enriched or depleted. (**d**) Representative Genome Browser
789 snapshots of regions analysed in (c). **(e, f)** Relationship between *SPOP*-mutant and *FOXA1*-mutant
790 subclasses of PRAD. **(e)** Classification of PRAD using the *SPOP*-mutant transcriptional classifier
791 (Liu et al., 2018). *FOXA1* mutations are depicted in blue (FKHD – DNA binding domain), green
792 (N-terminal domain) and black (truncations after FKHD domain). **(f)** Gene copy number profiles
793 of these molecular subclasses of PCa.
794

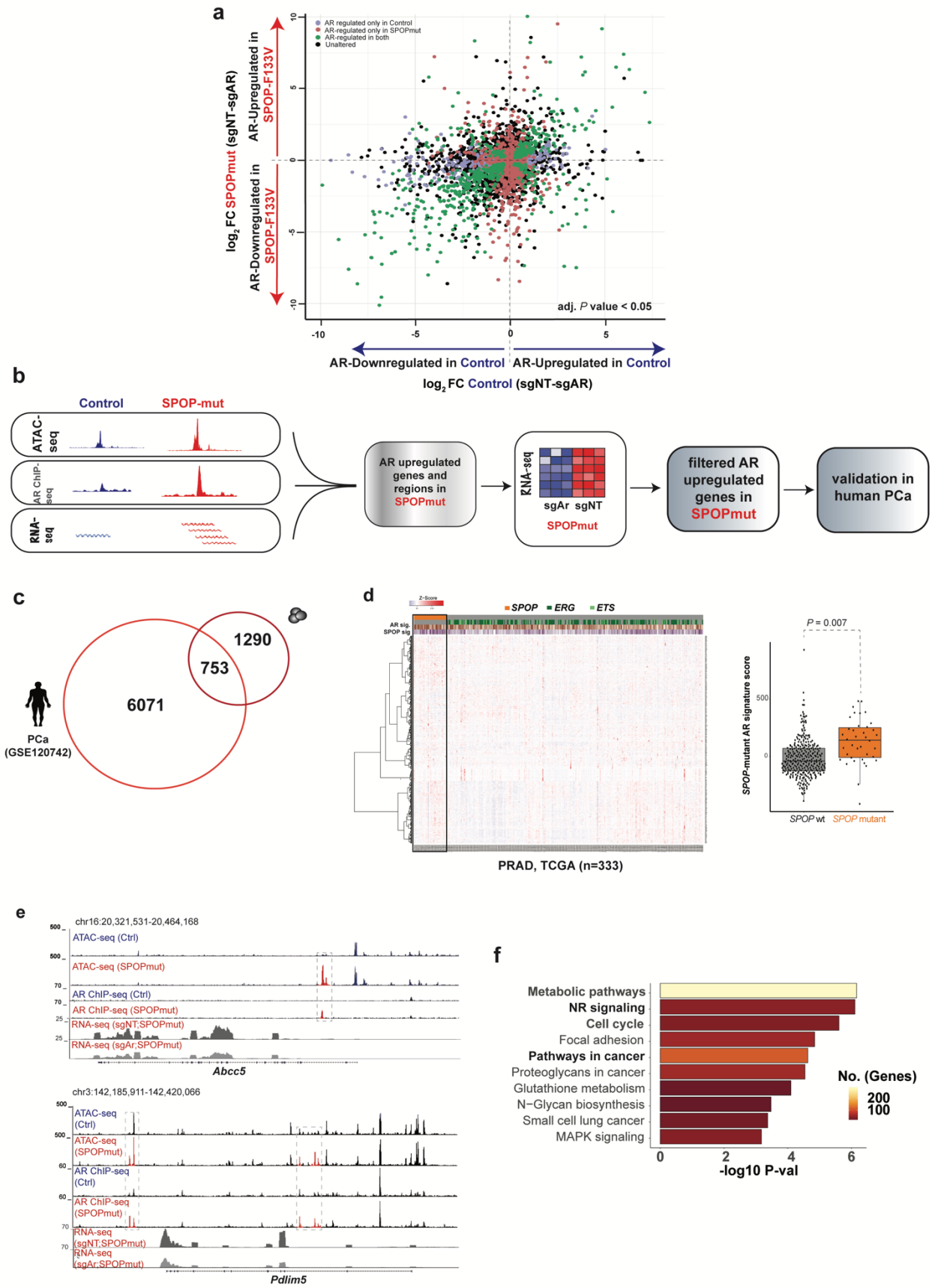
a
AR regulated only in Control
AR-regulated only in SPOPmut
AR-regulated in both
Unaltered
log2FC SPOPmut (sgNT-sgAR)
AR-Upregulated in SPOP-F133V
AR-Downregulated in SPOP-F133V
adj. P value < 0.05
AR-Downregulated in Control
AR-Upregulated in Control
log2FC Control (sgNT-sgAR)
b
Control
SPOP-mut
ATAC-seq
AR ChIP-seq
RNA-seq
AR upregulated genes and regions in SPOPmut
RNA-seq
sgAr sgNT
SPOPmut
filtered AR upregulated genes in SPOPmut
validation in human PCa
c
1290
753
6071
PCa (GSE120742)
d
SPOP
ERG
ETS
AR sig.
SPOP sig
PRAD, TCGA (n=333)
P = 0.007
SPOP-mutant AR signature score
SPOP wt
SPOP mutant
e
chr16:20,321,531-20,464,168
ATAC-seq (Ctrl)
ATAC-seq (SPOPmut)
AR ChIP-seq (Ctrl)
AR ChIP-seq (SPOPmut)
RNA-seq (sgNT;SPOPmut)
RNA-seq (sgAr;SPOPmut)
Abcc5
chr3:142,185,911-142,420,066
ATAC-seq (Ctrl)
ATAC-seq (SPOPmut)
AR ChIP-seq (Ctrl)
AR ChIP-seq (SPOPmut)
RNA-seq (sgNT;SPOPmut)
RNA-seq (sgAr;SPOPmut)
Pdlim5
f
Metabolic pathways
NR signaling
Cell cycle
Focal adhesion
Pathways in cancer
Proteoglycans in cancer
Glutathione metabolism
N-Glycan biosynthesis
Small cell lung cancer
MAPK signaling
No. (Genes)
200
100
-log10 P-val

795

796 **Fig. 5.** Nominating novel AR-regulated genes in the context of SPOP mutation **(a)** Plot showing
797 differentially expressed genes (adj. *P* value < 0.05) regulated by AR in Control cells (x-axis; blue)
798 and *SPOP*-mut cells (y-axis, red). **(b)** GSEA hallmark enrichment of AR-responsive genes in
799 Control (blue) and *SPOP* mutant (red) cells with plotted GSEA NES values. **(c)** Computational
800 steps to identify AR-upregulated genes specific to *SPOP* mutant human and murine cells. **(d)**
801 Overlapping AR-regulated genes in *SPOP*-mutant human PCa (Stelloo et al., 2018) and murine
802 cells. **(d)** Heatmap - Gene expression (n=753) in human PRAD samples (Cancer Genome Atlas
803 Research, 2015). Boxplots – PCa samples with higher expression of nominated genes (n=753)
804 have higher *SPOP*-mutant signature score. **(e)** Representative Genome Browser tracks of AR-
805 regulated regulatory regions and transcripts in *SPOP*-mut organoids. **(f)** Functional enrichment of
806 androgen-induced genes in murine *SPOP* mutant cells.
807

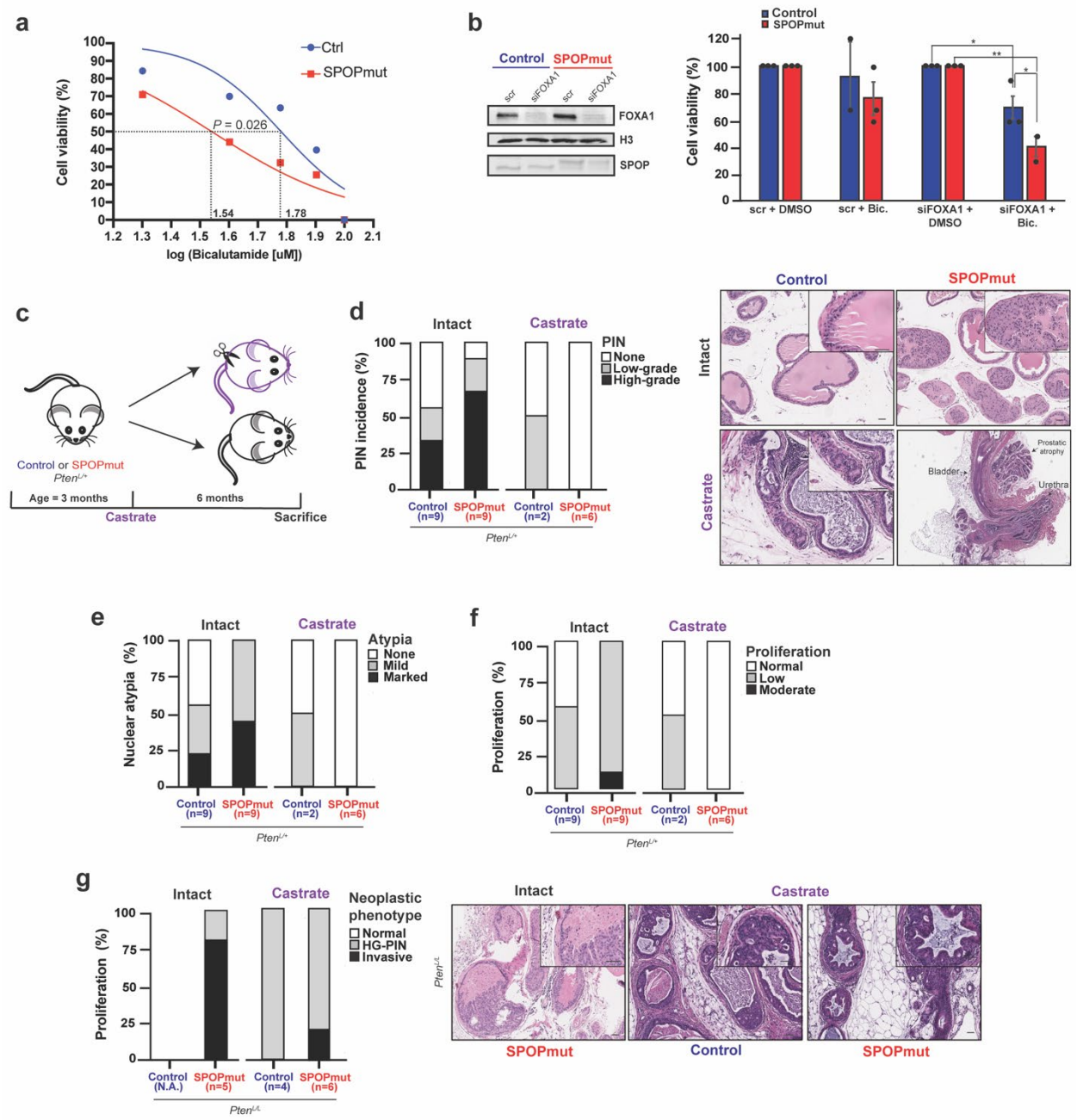

Fig. 6. The distinct phenotype of *SPOP* mutations shows dependency on functional AR signaling. **(a)** The dose-response curve (log scale) of Control and SPOPmut murine prostate organoids in response to bicalutamide. **(b)** Immunoblot of control and SPOPmut murine prostate cells after siRNA-mediated downregulation of FOXA1 (top) and cell viability of these cells after 20 μM bicalutamide treatment (bottom). **(c)** Schematic of castration experiment. **(d-f)** Incidence of PIN,

814 nuclear atypia and degree of proliferation in Control and SPOPmut mice before and after
815 castration. Representative H&E images are shown on the right and in Fig S5c-d. Scale bar, 50 mm.
816 **(g)** Incidence of neoplastic phenotypes (HG-PIN and invasive features such as necrosis, stromal
817 response and/or frank invasion) in Control and *SPOP-F133V* mice with representative images
818 shown on the right. Scale bar, 50 mm.

819

Figure 6

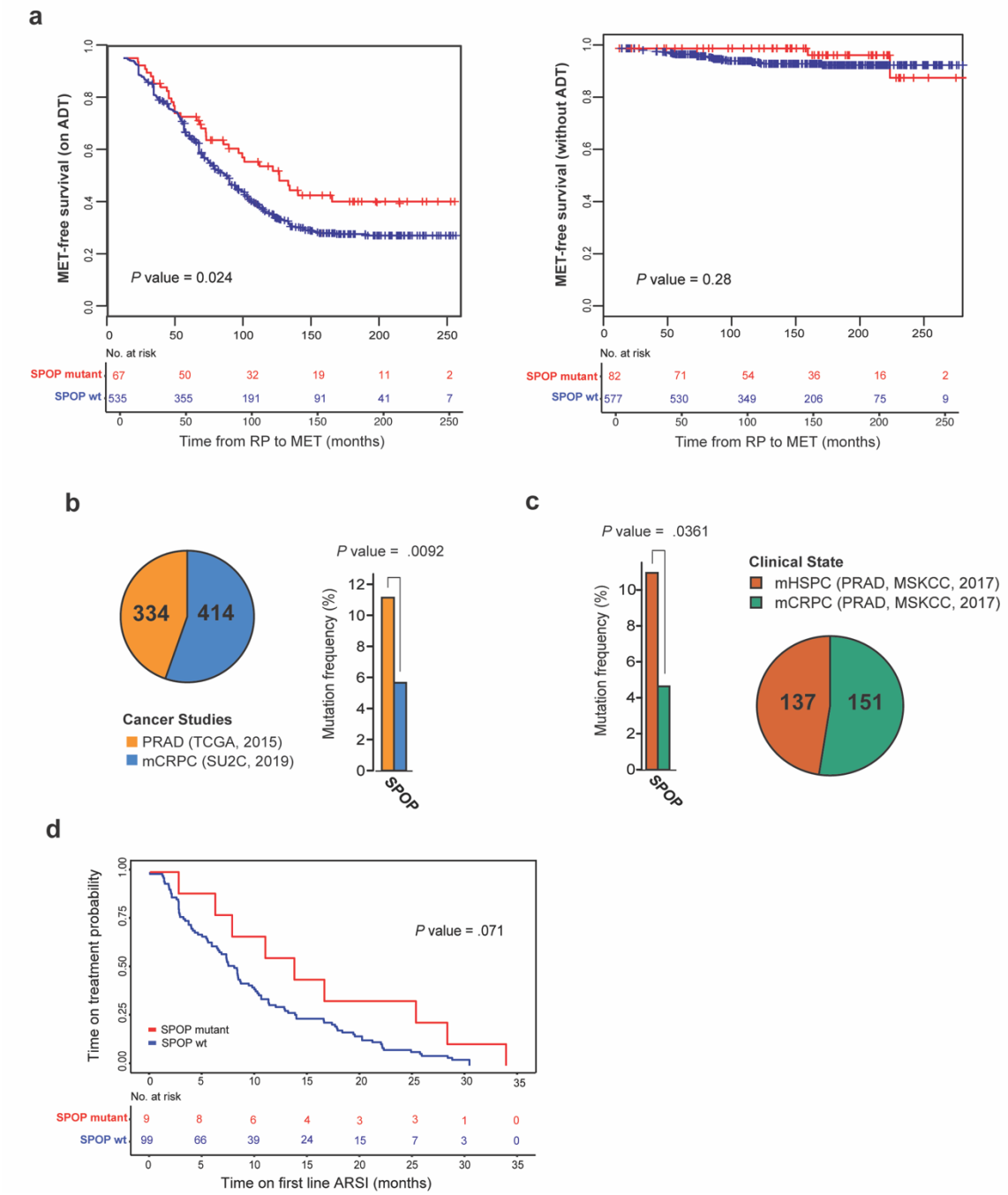

Fig. 7. Sensitivity of *SPOP* mutant PCa to therapies targeting AR signaling. **(a)** Significant clinical outcome difference between *SPOP* mutant and wild-type PCa via Kaplan-Meier analysis of metastasis (MET)-free survival for patients on androgen deprivation therapy (ADT) (left) or

824 without receiving ADT (right). **(b)** The occurrence of *SPOP* mutation in primary PCa (Cancer
825 Genome Atlas Research, 2015) and metastatic (mCRPC) samples (Abida et al., 2019). **(c)** When
826 metastatic prostate tumors (Abida et al., 2017) are compared – the hormone-sensitive ones
827 (mHSPC) have a higher frequency ($p < 0.0361$) of *SPOP* mutation than the resistant (mCRPC)
828 ones. **(d)** Kaplan-Meier analysis of *SPOP* wild-type and *SPOP*-mutated mCRPC tumors (27)
829 showing time on treatment with first-line androgen signaling inhibitors (ARSI).
830

831 **Supplementary Data**

832 Fig. S1. Distinct changes in androgen-induced chromatin and transcriptional landscape of normal
833 murine prostate cells.

834 Fig. S2. Androgen-dependent and independent chromatin remodelling of murine prostate cells
835 upon introduction of *SPOP* mutation.

836 Fig. S3. AR cistrome from *SPOP* mutant cells is enriched for FOXA1 and HOXB13 motifs.

837 Fig. S4. RNA-seq quality control.

838 Fig. S5. Murine SPOPmut prostate cells are more sensitive to anti-androgen treatment.

839 Table S3. Patient's characteristics from Decipher retrospective cohort.

840

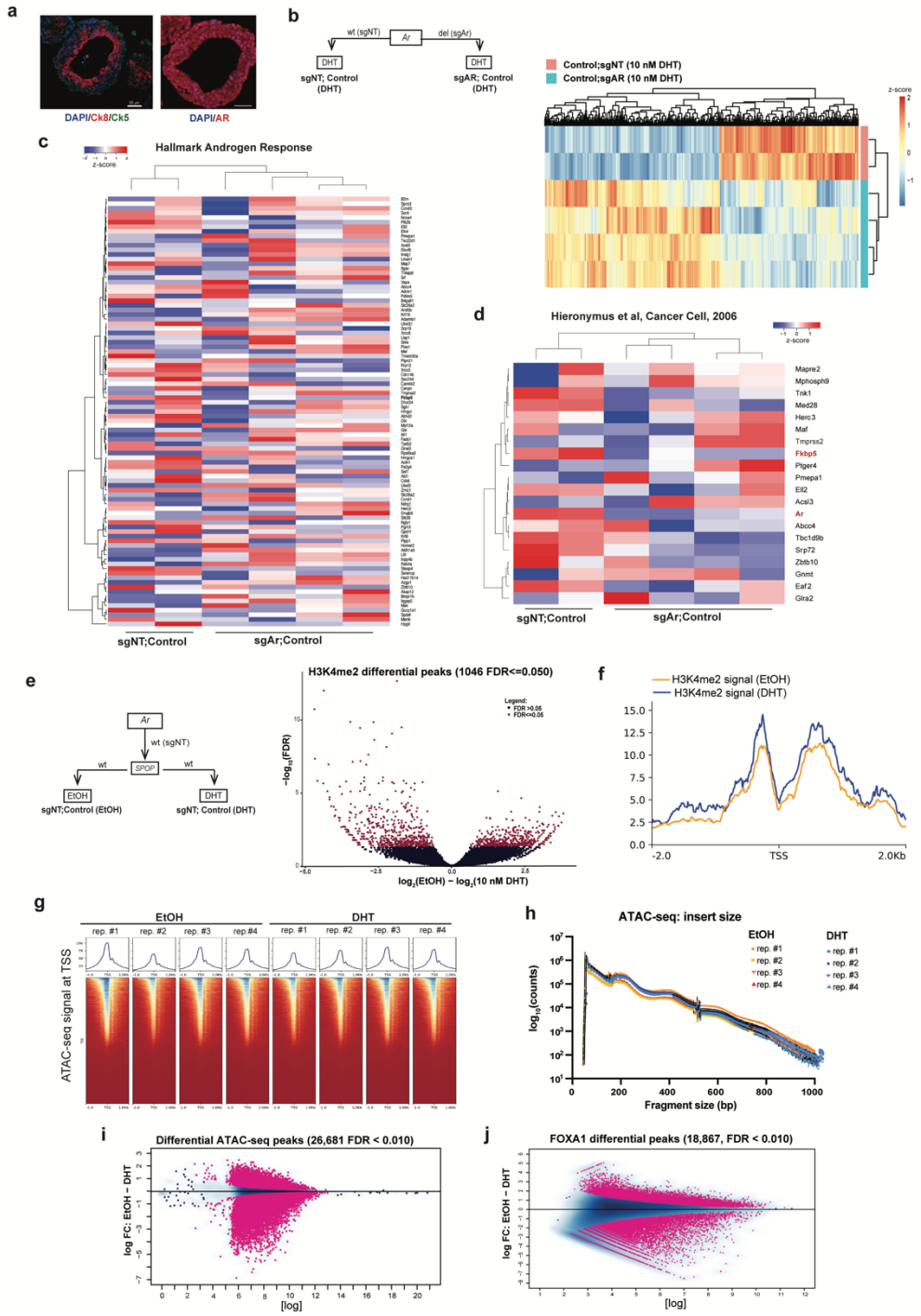

Fig. S1. Distinct changes in androgen-induced chromatin and transcriptional landscape of normal murine prostate cells (wildtype SPOP). **(a)** Morphology of murine prostate organoids (left: IF for Ck5 and Ck8) expressing AR (right). **(b)** Schematic representation of RNA-seq experiment and the heatmap showing all the differentially expressed genes. **(c, d)** Response of human AR-target

genes, from GSEA **(c)**, and literature (Hieronymus et al., 2006) **(d)**, to Ar downregulation in normal murine prostate organoids. **(e)** Schematics of the ChIP-seq and ATAC-seq experiments (left). Right – Volcano plot showing dynamics H3K4me2 ChIP-seq peaks at FDR 0.05. **(f)** H3K4me2 signal at the promotors of the AR-upregulated genes in Control organoids (shown in Figure 1c). **(g)** ATAC-seq quality metrics - distribution of DNA fragments in generated ATAC-seq libraries. **(h)** ATAC-seq quality metrics – enrichment of ATAC-seq signal at the transcription starts sites (TSS) of housekeeping genes. **(i)** Dynamic ATAC-seq peaks at FDR 0.01. **(j)** Dynamic FOXA1 ChIP-seq peaks at FDR 0.01.

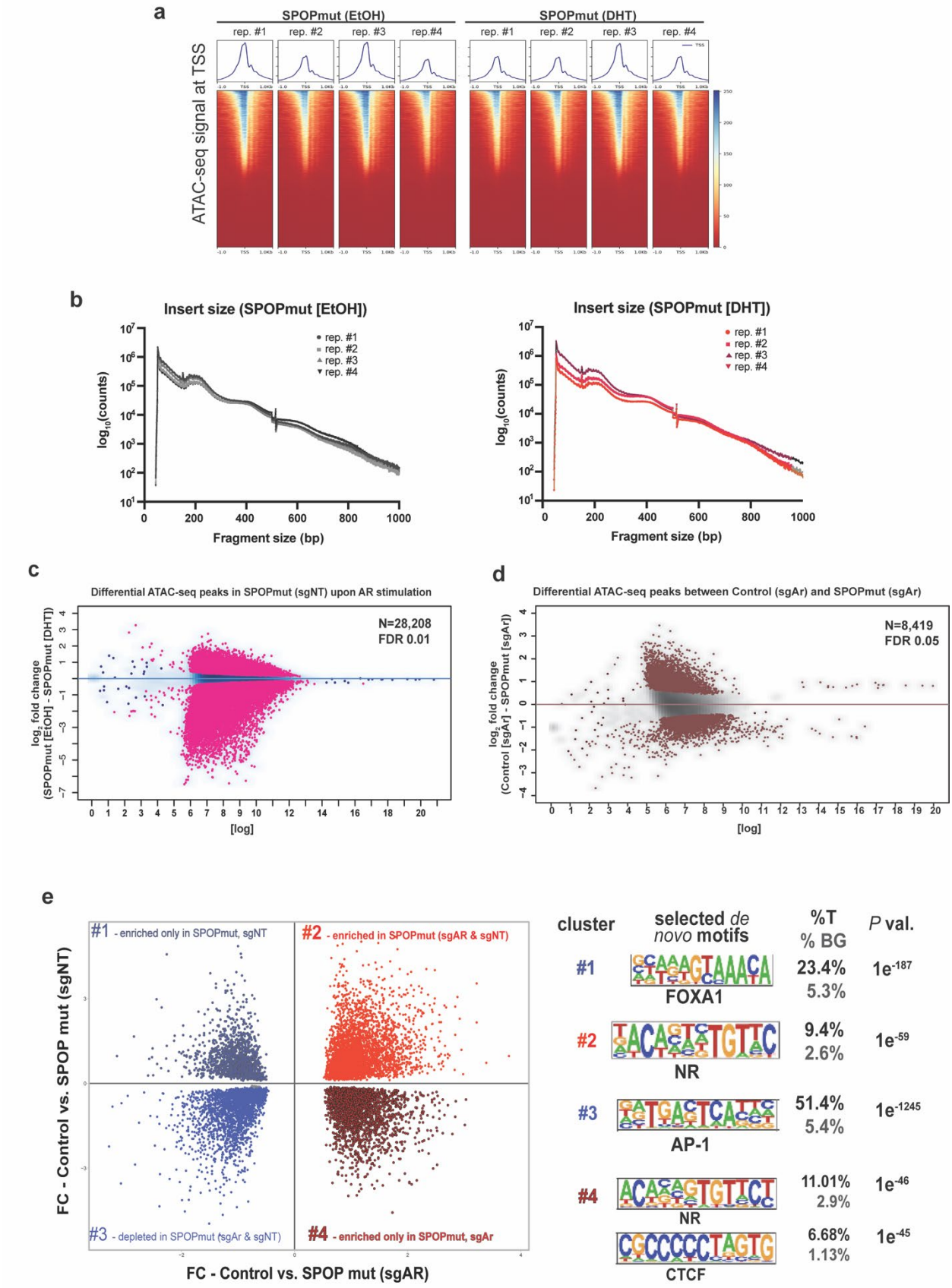
a
SPOPmut (EtOH)
SPOPmut (DHT)
rep. #1
rep. #2
rep. #3
rep.#4
ATAC-seq signal at TSS
b
Insert size (SPOPmut [EtOH])
Insert size (SPOPmut [DHT])
log10(counts)
Fragment size (bp)
c
Differential ATAC-seq peaks in SPOPmut (sgNT) upon AR stimulation
N=28,208
FDR 0.01
log2 fold change (SPOPmut [EtOH] - SPOPmut [DHT])
[log]
d
Differential ATAC-seq peaks between Control (sgAr) and SPOPmut (sgAr)
N=8,419
FDR 0.05
log2 fold change (Control [sgAr] - SPOPmut [sgAr])
[log]
e
#1 - enriched only in SPOPmut, sgNT
#2 - enriched in SPOPmut (sgAR & sgNT)
#3 - depleted in SPOPmut (sgAr & sgNT)
#4 - enriched only in SPOPmut, sgAr
FC - Control vs. SPOP mut (sgNT)
FC - Control vs. SPOP mut (sgAR)
cluster
selected de novo motifs
%T
% BG
P val.
#1
FOXA1
23.4%
5.3%
1e-187
#2
NR
9.4%
2.6%
1e-59
#3
AP-1
51.4%
5.4%
1e-1245
#4
NR
11.01%
2.9%
1e-46
CTCF
6.68%
1.13%
1e-45

855

856 **Fig. S2**. Androgen-dependent and independent chromatin remodeling of murine prostate cells
857 upon introduction of *SPOP* mutation. **(a, b)** Results of Encode quality metrics for ATAC-seq on
858 *SPOP* mutant cells (sgNT) before and after DHT treatment - enrichment at the promoters (i.e. TSS)
859 **(a)** and fragment size distribution **(b)**. **(c)** MA plot – dynamic accessible region upon AR
860 activation. **(d)** MA plot – dynamic regulatory regions induced by *SPOP* mutation when Ar is
861 downregulated. **(e)** Scatter plot – common and unique accessible regions in SPOP mutant cells
862 upon lower Ar expression. Right: results of de novo motif analysis. Black - target regions (%T).
863 Grey - background regions (%BG).
864

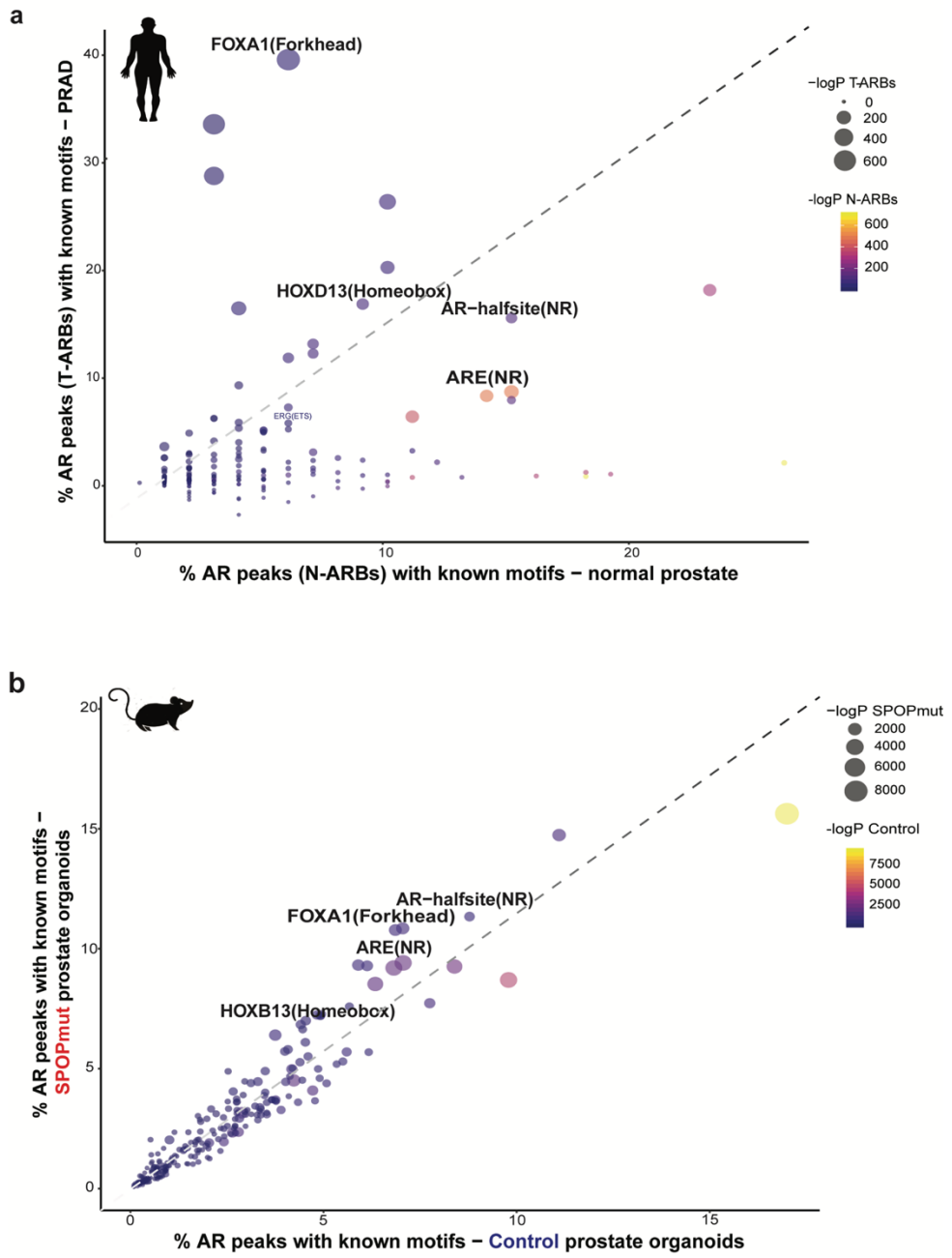

Fig. S3. AR cistrome from *SPOP* mutant cells is enriched for FOXA1 and HOXB13 motifs. **(a)** Comparison of the motifs found in AR peaks in normal human prostate tissues and cancers (Pomerantz et al., 2015). **(b)** Motifs found in AR bound regions in before and after introduction of SPOP mutation in normal murine prostate cells.

871

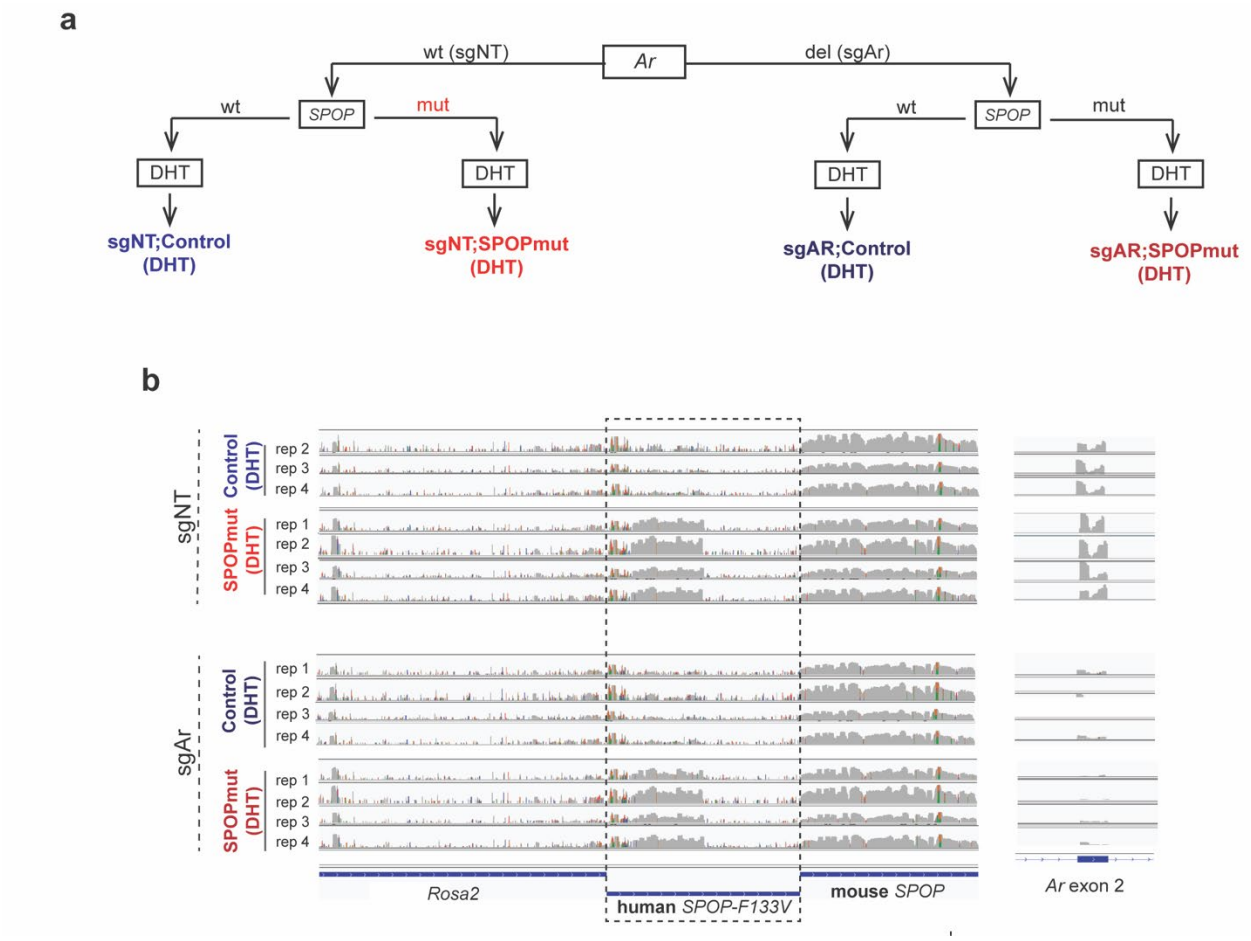

872

873 **Fig. S4.** RNA-seq quality control. **(a)** Schematic representation of all the generated RNA-seq

874 libraries. **(b)** Quality controls of the data – reads were aligned to human SPOP sequence (left)

875 and the Ar exon 2 (sgAr target).

876

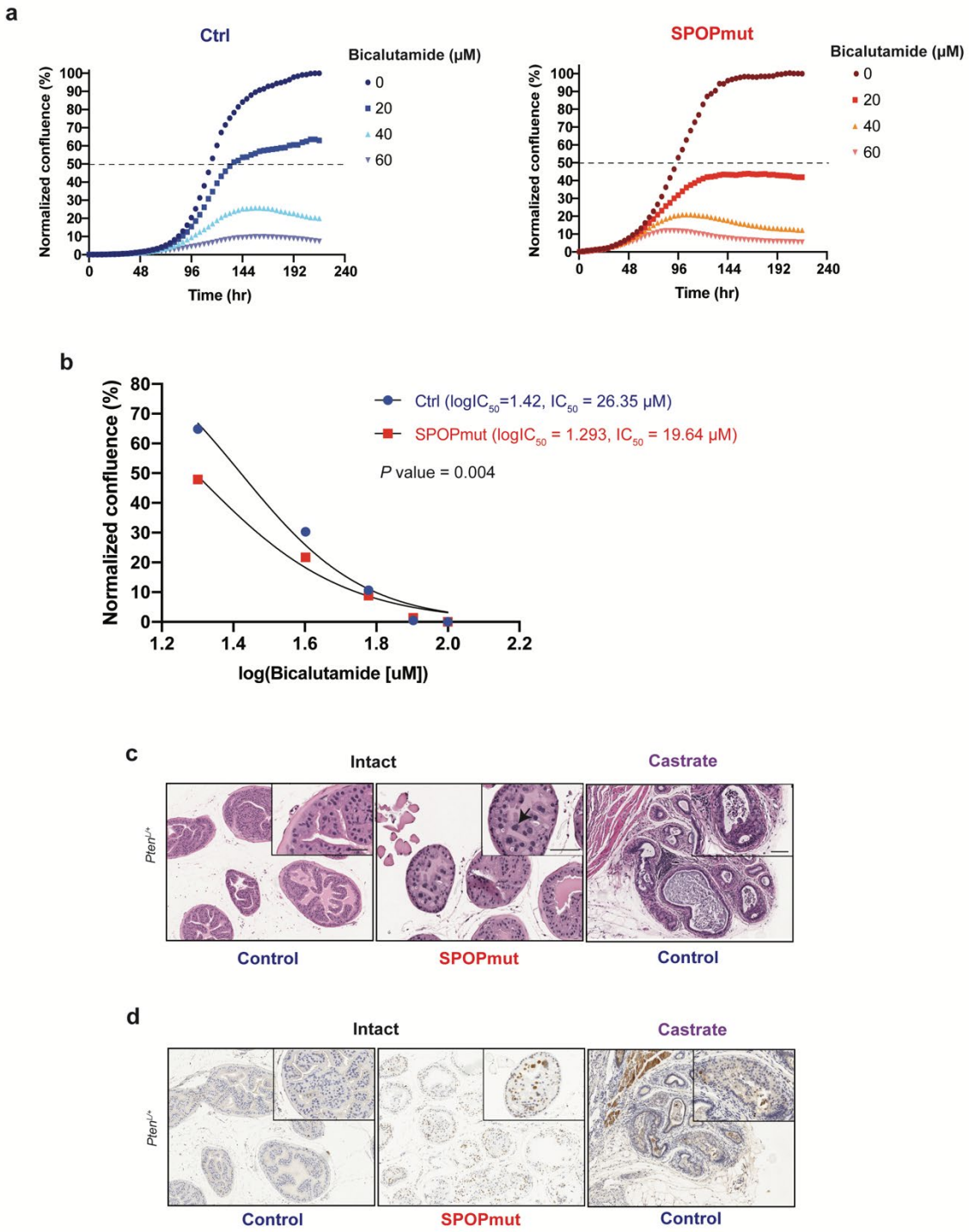

Fig. S5. Murine SPOPmut prostate cells show higher sensitivity to anti-androgen treatment. **(a, b)** Slower proliferation of *SPOP*-mutant cells when treated with bicalutamide in 2D (a) and 3D (b). **(c-d)** Representative images showing nuclear atypia and H&E staining.

Table S3. Patient's characteristics from Decipher retrospective cohort used for analysis in Fig.7a.

	***SPOP* mutant**	***SPOP* wild-type**
Cases	168	1,458
Median age (range)	65 (44-77)	62 (37-83)
Median PSA (range)	8.9 (1.9-87)	8.6 (0.1-201)
Gleason score (range)		
<=6	16	176
3+4	30	381
4+3	24	175
>=8	60	589
Pathological tumor stage		
pT2	66	464
pT3/4	82	722
Extracapsular extension	88 (53%)	855 (61%)
Lymp node invasion	20 (12%)	228 (16%)
Seminal vesicle invasion	35 (21%)	452 (32%)
Surgical margin	68 (41%)	703 (49%)

881